Petrogenesis of the ~2.77 Ga Monts de Cristal Complex, Gabon: evidence for direct precipitation of Pt- arsenides from basaltic magma

WD Maier, School of Earth and Ocean Sciences, Cardiff University, UK (corresponding author)

B Rasmussen & I Fletcher, Curtin University, Australia

B Godel, SJ Barnes & LA Fisher CSIRO, Perth, Australia

Shenghong Yang, Department of Geosciences, University of Oulu, Finland

H Huhma & Y Lahaye, GTK, Espoo, Finland

Running title: Petrogenesis of the Monts de Cristal Complex, Gabon

ABSTRACT

The Monts de Cristal Complex of Gabon consists of several igneous bodies interpreted to be remnants of a tectonically dismembered, > 100km long and 1-3 km wide, ultramafic-mafic intrusion emplaced at 2765-2775 Ma. It is the most significant mafic-ultramafic layered complex yet identified on the Congo craton. The Complex consists largely of orthopyroxenite cumulates, with less abundant olivine-orthopyroxenites and norite, and rare harzburgites and dunites. Mineral compositions (Fo_{ol} 84, $Mg\#_{Opx}$ 85, An_{plag} 60-68, Cr/Fe chromite 1-1.45) and whole rock data suggest that the magma was a low-Ti basalt containing approximately 10% MgO and 0.5% TiO_2. Trace element and Rb-Sr and Sm-Nd isotope data indicate the presence of an enriched component, possibly derived from crustal contamination of a magma generated in the sub-lithospheric mantle. Most rocks

show a highly unusual pattern of strong Pt enrichment (10-150 ppb) at low concentrations of Pd (1-15 ppb), Au (1-2 ppb), Cu (1-20 ppm), and S (<500 ppm) suggesting that, unlike in most other PGE rich intrusions globally, platinum in the Monts de Cristal Complex is not hosted in magmatic sulfides. Synchrotron X-ray fluorescence mapping revealed the location of buried small Pt particles, most of which are associated with As. We propose that this constitutes some of the strongest evidence yet in support of magmatic crystallization of a Pt-As phase from S undersaturated magma.

Keywords: Gabon; layered intrusion; platinum-group elements; Pt arsenide; synchrotron

INTRODUCTION

The Monts de Cristal (MdC) Complex, locally also referred to as the Kinguele Complex, is located in NW Gabon, some 70-150 km to the NE of Libreville, and ~50-100 km north of the Equator (Fig. 1a). It forms a tectonically dismembered intrusion, ~100 km in length and mostly ~1-3 km wide (Fig. 1b), constituting the largest mafic-ultramafic layered intrusion so far discovered on the Congo craton. In terms of its inferred shape and the observed lithologies, it bears some resemblance to the PGE mineralized Great Dyke of Zimbabwe. Based in part on these analogies, several companies have conducted exploration for chromite seams and PGE reefs in the MdC during the last decades. After initially obtaining promising exploration indicators, namely elevated Pt concentrations across most of the strike of the Complex, it was ultimately realized that the Pt is not associated with cumulus magmatic sulfide, in contrast to economic PGE reefs elsewhere. However, the strong enrichment of Pt relative to Pd in the MdC is of considerable

47 petrological significance, in that it constitutes the most convincing case yet identified for
48 direct precipitation of Pt phases from basaltic magma. In the present paper, we provide a
49 description and compositional characterization of these unique Pt enriched rocks and
50 suggest a model for their formation.
51
52 **REVIEW OF PREVIOUS WORK**
53 The first account of mafic rocks in the MdC area was published by Arsandaux (1912)
54 who reported the presence of ophitic gabbros associated with charnockite to the south of
55 Kinguele. Noritic massifs were first indicated in the Libreville Est geological map of
56 1959 (Aubague and Hausknecht, 1959), but reconnaissance mapping of the intrusion only
57 began in the 1980s when the Direction Générale des Mines et de la Géologie du Gabon,
58 in collaboration with the French Bureau de Recherches Géologiques et Minières, carried
59 out a regional mineral assessment comprising airborne geophysical suveys and stream
60 geochemistry over an area of ~100.000 km^2. This program identified Archaean granite-
61 gneiss basement rocks containing banded iron formation, amphibolites as well as
62 gabbronoritic intrusives. The presence of ultramafic intrusives was first indicated in the
63 1:200 000 Kango geological sheet (Kassa-Mombo et al., 1988). Mineral exploration
64 activities initially focused on chromite, but no massive seams were found and the detrital
65 chromite grains turned out to be too Fe- and Al-rich to be of economic interest
66 (Campiglio et al., 1983). Reconnaissance geochronological work indicated an age of ~
67 2.78 Ga (2777±83 Ma, Rb-Sr on whole rocks, 2783±77 Ma, Pb-Pb on whole rocks, Caen-
68 Vachette et al., 1988).

In 2002, Southern Era Resources Limited started an exploration program for PGE in the MdC, comprising mapping, comprehensive stream sediment sampling, and soil sampling. Significant Pt anomalies closely associated with all blocks of the intrusion were delineated and a large number of outcrop samples were collected for high-precision geochemistry and geochronology (Maier, 2004). The exploration licence was acquired by Lonmin in 2005 which carried out extensive soil sampling at KG1, KG1 extension and KG3, and remapped some of the bodies (Prendergast, 2009). The company also drilled 15 diamond drill holes (13 holes at KG1 and two holes at KG3). In addition, a detailed magnetic-radiometric survey was conducted by Fugro Airborne Surveys in 2008.

ANALYTICAL METHODS

Whole rock and mineral chemistry

Seventy five outcrop samples were analysed for major and minor elements as well as a range of lithophile trace elements including Sr, Rb, Nb, Y, Zr, Ni, Cu, Zn, Co, Cr, Sc, V and REE using ICP-MS at Cardiff University, UK, after grinding to <75 μm in agate ring and ball mills. The concentrations of the PGE were determined using ICP-MS after nickel sulfide fire assay and tellurium co-precipitation, on 15 g aliquots. Full details of the analytical procedures used are given in McDonald and Viljoen (2006). The analytical procedure was validated by frequent analysis of reagent blank samples, replicate samples and reference materials (Electronic Appendix 1). All whole rock data are listed in Electronic Appendix 2, and average compositions of rocks types are given in Table 1. In addition to the outcrop samples, Lonmin analysed ~2000 samples from 13 drillcores for Pt, Pd and Au as well as selected major (Fe, Mg, Al, Ca), minor (Ti, Mn) and trace

92 elements (Cr , Ni, Cu, Co, V, Zn, S, and Zr), at Genalysis, Johannesburg, using Pb-
93 collection fire assay followed by mass spectrometry for Pt, Pd and Au, and ICP-OMS for
94 a range of other major and trace elements. The Pt contents and the Pt/Pd ratios from the
95 commercial lab show good overlap with the ICP-MS PGE data, suggesting the 2 methods
96 have broadly similar accuracy (Maier, 2009).
97 *In situ* Sr isotope analyses of plagioclase were performed by Laser ablation ICP-
98 MS using a Nu Plasma HR multi-collector inductively coupled plasma mass spectrometry
99 (MC-ICP-MS) and a Photon Machine Analyte G2 laser microprobe at the Geological
100 Survey of Finland in Espoo. Analytical details are given in Yang et al. (2013), and the
101 complete data are provided in Electronic Appendix 3.
102 Whole rock Nd isotopes were also determined at GTK in Espoo. Analytical
103 details are given in Huhma et al. (2012), and data for 5 samples are provided in
104 Electronic Appendix 4.
105 The compositions of orthopyroxene, olivine, plagioclase and chromite were
106 determined in 5 samples of (olivine)orthopyroxenite, 1 sample of norite, and 2 samples of
107 gabbro from the KG1 and KG3 blocks (Electronic Appendix 5-8). The instrument used
108 was a JEOL JXA-8200 electron microprobe at the University of Oulu, operated at an
109 accelerating voltage of 15 kV and a beam current of 30 nA. The accuracy of analyses was
110 monitored using reference material of similar composition. The reproducibility varied by
111 less than 2 %.
112
113 **Synchrotron X-ray fluorescence microscopy**

X-ray fluorescence microscopy using synchrotron radiation is a highly effective technique for locating ultra-trace high-Z components, owing to the effective penetration of the x-ray beam and the fluoresced target x-rays through sample volumes. A protocol has been developed for searching for micron-scale precious metal (Au, PGE) enriched grains within geological materials (Ryan et al. 2014). X-ray fluorescence microscopy (XFM) was performed on the XFM beamline at the Australian Synchrotron in Melbourne (Paterson et al., 2011) using the Kirkpatrick Baez mirror microprobe end-station. This provides a monochromatic 2 µm beam-spot size for energies in the range 4-20 keV. Equipped with the Maia 384 detector array, the XFM beamline can acquire images at 2 µm resolution over areas of several square centimetres (Kirkham et al., 2010; Ryan et al., 2010a) with count rates of ~ 4-10 M/s and energy resolution of 300-400 eV. In this study, large area element maps were collected on 100 micrometer thickness polished thin sections backed by 1millimetre quartz glass slides with a beam energy of 18.5 keV, spot size of 2µm and a dwell times per pixel of 0.97 milli-second to locate areas where Pt-rich inclusions were observed. For each sub-area identified, additional maps were collected with longer dwell time (15.26 millisecond per pixel) to enhance the signal to noise ratio and improve further quantification. Each dataset was analysed with the GeoPIXE software suite which uses a fundamental parameters approach, with spectral deconvolution and imaging using the Dynamic Analysis method (Ryan, 2000; Ryan et al., 2010c) and a detailed model of Maia detector array efficiency (Ryan et al., 2010b). Data were fitted using a yield file which calculates the effects of X-ray absorption by the given matrix or mineral phase (Ryan, 2000). Element maps were produced after spectra were fitted and a dynamic analysis matrix file produced. Platinum abundance was

measured using the Lα line. These maps were then interrogated to confirm the presence of Pt and identify associated elements and phases. It must be noted that this method samples potentially the entire 100 micrometer thickness of the section, and thus Pt may be sitting on a buried grain boundary even if it appears within a grain. The true nature of the grain location is difficult to resolve without milling down to the grain, but it is possible to further interrogate the spectra to gain a rough quantification of probable depth in the sample to assist with this. The correct identification of Pt has been confirmed by matching XFM maps collected using this methodology with Pt phases identified at the sample surface by optical microscopy in sulfide ore samples (Barnes et al., 2011), although as yet we have not identified any optically visible Pt phases in the Monts de Cristal samples. Identification of Pt phases in Monts de Cristal samples has been confirmed by high resolution PIXE imaging (Barnes et al., in prep).

Geochronology

Examination of orthopyroxenite samples Px12, Px39 and 1290 by scanning electron microscope revealed the presence of four U-Pb geochronometers: baddeleyite, zircon, zirconolite and monazite (Electronic Appendix 9). However, zircon grains appeared to have been affected by radiation damage and zirconolite was largely destroyed by secondary alteration, rendering both unsuitable for dating. Baddeleyite and monazite were viable for ion microprobe geochronology but the small size and limited number of grains constrain the data quality. Crystals of both minerals >10 µm in size were drilled

159 from polished thin sections in ~3 mm platelets and mounted in 25 mm resin disks for ion
160 microprobe (SHRIMP) analysis.

161 Baddeleyite was analysed using a ~0.15 nA O2- primary ion beam focused on a
162 <10 µm spot. A chip of Phalaborwa (2060 Ma) baddeleyite was mounted with the
163 samples for Pb/U calibration and as a monitor of Pb isotope data quality. Monazite
164 analyses used a ~10 µm, 0.25 nA primary ion beam. Monazite reference samples (French,
165 PD-95, z2234 and QMa28-1) were in a separate mount that was cleaned and Au-coated
166 with the sample mount. Baddeleyite data acquisition and reduction followed the
167 procedures of Wingate et al. (1998). Monazite procedures were those of Fletcher et al.
168 (2010). Primary data reduction was performed using Squid-2 software (Ludwig, 2009),
169 using "spot average" data for all ratios. Corrections to monazite data for matrix effects in
170 Pb/U and Pb/Th, and a small correction for instrumental mass fractionation were applied.
171

172 **STRUCTURE AND LITHOLOGIES**

173 The MdC is largely hosted by Archaean basement rocks comprising granite-gneiss and
174 greenstones. The basal contacts of the intrusions dip steeply towards the centres of the
175 intrusive blocks (~80°) and are defined by aphanitic margins, grading inwards to
176 medium-grained norite, orthopyroxenite and, less abundantly, harzburgite and dunite
177 (Edou Minko et al., 2002). In addition, the Southern Era and Lonmin exploration
178 programs discovered isolated anorthosite layers and several occurrences of ophitic
179 gabbro, the latter located near the margins of the KG1 and KG3 blocks. All mafic-
180 ultramafic rocks are generally poorly layered and lack distinct differentiation cycles. The
181 norites appear to form lenses within the orthopyroxenites rather than distinct, laterally

182 persistent, layers. In addition, norites appear to be relatively common towards the basal
183 contact of the intrusions, e.g., at KG3 (drill core MPD 015) and at KG1 (drill cores MPO-
184 03 and 04). Xenoliths of the country rocks, consisting mainly of feldspar-rich
185 amphibolites as well as less abundant felsic fragments, have been intersected in several
186 boreholes at the KG1 intrusive block.

187 The most comprehensive information on the geology of the Complex is available
188 from KG1, where an extensive soil geochemical program was conducted (Prendergast,
189 2009). The location of the grab samples analysed by us, and some of the bore holes
190 drilled by Lonmin in 2007-2008 are indicated in Fig. 2. The KG1 mafic-ultramafic body
191 measures ~ 8 km by 2 km and appears to consist of two distinct blocks (Prendergast,
192 2009; Fig. 2). In the west and north, the intrusion is hosted by felsic gneisses and mafic
193 schists interpreted to represent a granite-gneiss-greenstone terrane. Tonalitic to
194 granodioritic granite gneiss containing intercalations of quartzite, amphibolite and
195 ultramafic slivers occurs to the south and east of the body. Proterozoic clastic and
196 chemical sedimentary rocks occur to the west of an inferred N-NE trending fault, 1-2 km
197 west of KG1. Most contacts of the intrusion with its host rocks are tectonic (Prendergast,
198 2009), but the intrusive basal contact of the body has been intersected by drill cores
199 MPD-03 and 04 (Fig. 2). This intrusive contact consists of a 1-2 m aphanitic rock
200 interpreted as a chilled margin that grades to orthopyroxenite (Electronic Appendix 10).
201 Based on the concordance of the strike of layering with the NW flank of the intrusion,
202 Prendergast (2009) proposed that the intrusive contact strikes SW-NE and dips at ~60° to
203 the SE, and that the total stratigraphic thickness is ~1700 m. The dip of layering in most

of the remainder of the Complex remains unclear, due to weathering and paucity of layering.

The rocks of the KG1 block are mainly massive orthopyroxenites. Norites appear to be relatively abundant along the south-central margin, whereas olivine pyroxenite and occasional harzburgite predominantly occur in the east, consistent with elevated Ni values in soil sediment surveys. In drill core MPD-03 there is a ~ 400 m basal reversal expressed by a downward decrease in grain size together with an increase in modal plagioclase and biotite, relatively prevalent orthocumulate textures, several noritic intervals, occasional acicular textures, and enclaves of felsic melt rock. In another drill core (MPD-01), relatively fine grained orthopyroxenite overlying the floor contains xenoliths of amphibolite. All segments of the MdC intrusion are cut by abundant amphibolized plagioclase-clinopyroxene-phyric dolerites of unknown age.

PETROGRAPHY

The ultramafic rocks are mostly heteradcumulates or mesocumulates with between ~5 and 15% intercumulus material (Fig. 3a-c). Orthocumulates are less abundant and mainly confined to the stratigraphically lower portions of the intrusion. Considering the Archean age of the Complex, most rocks are remarkably unaltered. Minor to moderate serpentinization and chloritization is observed predominantly in the olivine-bearing lithologies. Orthopyroxene is mostly up to 2 mm in size, commonly of euhedral or subhedral habit (Fig. 3b-c), and aligned sub-parallel to the layering. Olivine forms anhedral grains up to 4 mm in width that can be moderately altered to serpentine and magnetite. Plagioclase occurs as either intercumulus, poikilitic or, in places, cumulus

grains. In the orthopyroxenites, chromite tends to be rare, forming occasional clusters and chains of very small (< 0.01mm) euhedral and subhedral crystals included in orthopyroxene (Fig. 3d-e). Chromite is slightly more abundant in olivine pyroxenites, where grains tend to be larger (up to 0.1 mm) and may occur within, or interstitial to, orthopyroxene. Clinopyroxene is relatively rare as an interstitial phase (mostly < 1-2 modal%), but commonly forms exsolution lamellae and blebs in orthopyroxene. Phlogopite is a common accessory phase and may constitute up to 2 modal % in some samples. Hornblende, tremolite and actinolite are accessory phases, largely related to alteration. Sulfides form small grain aggregates up to about 20 microns in size mostly located on orthopyroxene grain boundaries and consist of pyrrhotite, pentlandite and chalcopyrite. Notably, many orthopyroxenes are distinctly zoned showing dark rims (Fig. 3c). Synchrotron X-ray fluorescence mapping has shown the rims to be Ti enriched. The absence of residual phases such as apatite, amphibole or K-feldspar implies that the last few percent of trapped liquid was completely expelled from the rock during heteradcumulate formation, at least at the scale of a thin section.

Norites consist mainly of subhedral orthopyroxene and intercumulus or cumulus plagioclase. The latter forms tabular subhedral crystals up to 4 mm in length (Fig. 3f). Clinopyroxene is intercumulus and phlogopite, quartz and alkali feldspar are accessory phases. Chromite is rare, occasionally occurring as clusters of very small grains included in orthopyroxene, similar to the orthopyroxenites. Based on the above observations, the crystallization sequence of the exposed portion of the Monts de Cristal intrusion is ol+cr – opx – opx+pl - opx+pl+cpx.

Gabbros are represented by just two samples, one from KG3 (sample Dy18), and the other from KG1 west (sample Hz3). The rocks have a medium-grained ophitic texture, containing tabular, elongated plagioclase (up to 1 mm long) and anhedral or subhedral clinopyroxene (up to 2 mm) (Fig. 3g-h). Olivine is a minor phase, forming mostly relatively small (<1mm) anhedral crystals, but occasionally they occur as larger grains up to 1 cm across. Magnetite forms anhedral aggregates reaching up to 1-5 modal %. Sulfides comprise mainly pyrrhotite and chalcopyrite that form very small trace phases.

The amphibolites are fine to medium grained rocks. Plagioclase forms subhedral tabular crystals up to 2 mm long and < 1 mm wide. Amphibole grains tend to be anhedral or, in some cases, subhedral, forming pseudomorphs of pyroxene. Some samples have granular textures and are finer grained, suggesting metamorphic recrystallisation.

MINERAL CHEMISTRY

In general, the analysed MdC samples show relatively limited mineral compositional variation compared to other layered intrusions. Olivine has mostly 75-84 Fo and 2400-3600 ppm Ni, with one sample having 4400 ppm Ni. These Ni contents are higher than those of olivines with equivalent Fo contents in most other layered intrusions (Fig. 4). Orthopyroxene has Mg# 0.78-0.85, 200-1000 ppm Ni, 0.4-0.7% Cr_2O_3, and up to 2% Al_2O_3. Cumulus plagioclase has An 67, whereas intercumulus plagioclase has An 60-68. Chromite contains around 40% Cr_2O_3, and has Cr/Fe ~ 1 to 1.4. Norites have approximately similar mineral compositions as the orthopyroxenites.

Two samples of fine-grained ophitic gabbro from the margins of the intrusion have slightly less magnesian clinopyroxene (Mg#0.77-0.8) than the orthopyroxenites and norites. Plagioclase (An63-67) is of similar composition as in the norites, but olivine in the gabbros is significantly more iron-rich (Fo57-58) than in the other lithologies.

WHOLE ROCK CHEMISTRY

Lithophile elements

Concentrations of Al_2O_3, TiO_2, Cr, and Ni are plotted vs MgO in Figure 5a-d. The MdC orthopyroxenites and norites have between 15 and 32% MgO, whereas the ophitic gabbros have between 8.5-9% MgO. The concentrations of the major and minor elements are mainly controlled by the modal proportions of orthopyroxene, olivine, and plagioclase. Based on the lever rule, it is estimated that the proportion of olivine to orthopyroxene may reach up to ~20%, consistent with petrographic data. The composition of the trapped melt cannot be well constrained, except for TiO_2 where a best fit line through the ultramafic rocks indicates TiO_2 levels in the trapped melt of around 0.5 wt%. REE patterns of most samples are fractionated (Electronic Appendix 11), showing relative enrichment in LREE over HREE, but Gd/Lu_N <1. Only a few samples show slight positive or negative Eu anomalies. Incompatible trace element patterns show marked enrichment in LILE, positive Th anomalies, and negative anomalies in Nb-Ta and P (Fig. 6), indicating the presence of an enriched component in the rocks.

Trace element contents in the two gabbro samples are more than 5 times those in the orthopyroxenites and norites. Together with their ophitic texture, this suggests that the samples approach liquid compositions, either frozen against the margin of the intrusion or

294 emplaced as dykes or sills. The rocks have 47-48% SiO_2, 8.5% MgO, 12 % Fe_2O_3, 15%
295 Al_2O_3, 0.7-0.8% TiO_2, 2% Na_2O and 0.1-0.2% K_2O (Table 1). They can thus be
296 classified as Al-tholeiites. The multi-element patterns of the gabbros are much flatter and
297 less fractionated than those of the orthopyroxenites and norites (Fig. 6). The two samples
298 analysed have remarkably similar trace element patterns, considering that they were
299 collected from two different intrusive blocks located > 50 km apart. The patterns show
300 only subtle negative Nb-Ta anomalies, reminiscent of many Archean basalts (Barnes et
301 al., 2012). Zirconium contents of the gabbros are ~50ppm, in the range of Yilgarn low-Ti
302 basalts (Barnes et al., 2012), as are Cr and Ni contents (~400 and 200 ppm, respectively).
303 The amphibolite dykes also have relatively flat trace element patterns (Fig. 6h).
304 The concentrations of most incompatible trace elements are significantly elevated relative
305 to the orthopyroxenites and norites, by an order of magnitude. This is consistent with the
306 amphibolites representing liquids. The shape of the multi-element patterns is broadly
307 similar to those of the gabbros, except that the amphibolites have strong negative Sr
308 anomalies and are relatively more enriched in LILE. Furthermore, the amphibolites have
309 markedly higher total incompatible element concentrations than the gabbros.
310
311 **Sulphur and chalcophile elements**
312 The sulphur contents of the MdC cumulates are mostly < 100 ppm, consistent with the
313 paucity of sulphides in the thin sections. Sulphur shows a weak positive correlation with
314 TiO_2 (Fig. 7) suggesting that S behaved as an incompatible element during
315 crystallization. We can place some constraints on the S content of the parent magma by
316 means of the lever rule. The composition of the trapped melt can be delineated by a best

317 fit line through the whole rock compositions of the least evolved orthopyroxenites.
318 Assuming a TiO_2 content of ~0.4-0.5% for the liquid, as indicated by TiO_2-MgO
319 relationships (Fig. 6b), the S content of the magma is between 100 and 300 ppm. As the S
320 solubility of basaltic magmas at crustal pressure is on the order of 1000-2000 ppm
321 (Mavrogenes and O'Neill, 1999), the MdC magma is likely strongly S undersaturated.

322 Copper contents of the MdC orthopyroxenites and ol-pyroxenites are mostly
323 between 5 and 40 ppm (Electronic Appendix 12) showing a positive correlation with
324 TiO_2. This indicates that Cu behaved as an incompatible element during fractionation,
325 that the initial liquid (at 0.4-0.5% TiO_2) contained ~50-60 ppm Cu, and that the magma
326 did not equilibrate with sulphide melt during fractionation.

327 For the noble metals, two datasets are available, one being based on 75 outcrop
328 samples collected during the 2004 field season (Fig. 8), whereas the other is based on
329 several 1000 drill core samples analysed during 2007-2008 (Fig. 9-10 and Electronic
330 Appendix 13). The outcrop samples have up to 70 ppb Pt, but mostly <20 ppb Pd, <2ppb
331 Au, <6 ppb Rh, <9 ppb Ru, and <2ppb Ir. As expected, the PGE contents in the drill cores
332 cover a wider range extending to higher concentrations. The orthopyroxenites contain up
333 to ~ 150 ppb Pt, 25 ppb Pd, 4 ppb Ir, 9 ppb Ru, 6 ppb Rh, and 3 ppb Au. With the
334 exception of Pd and Au, the norites tend to contain lower PGE contents than the
335 orthopyroxenites, i.e., up to ~ 20 ppb Pt, 15 ppb Pd, 1 ppb Ir, 3 ppb Ru, 2 ppb Rh, and 3
336 ppb Au. Pd and Au show weakly developed negative correlations with MgO (Fig. 8a-b),
337 consistent with an incompatible behavior of the two noble metals. In contrast to Pd and
338 Au, the other PGE (Pt, Rh and the IPGE) show positive correlations with MgO (Fig. 8c-
339 f), indicating compatible behavior. Compatible behavior of the IPGE is not uncommon in

340 mafic-ultramafic rocks (Barnes et al., 1985), but compatible behavior of Pt is rare (Park
341 et al., 2013).

342 The drill core data show that the highest Pt values in unaltered rock are around
343 150 ppb (Fig. 9). These values occur in a specific layer that can be correlated laterally for
344 several 100m. Soil geochemistry (Prendergast, 2009) suggests that beyond that, the layer
345 either pinches out or is buried. Some strongly elevated Pt values are also observed within
346 the 2-20m lateritic cover where Cu and Cr also show anomalously high values (Fig. 10).
347 Notably, the highest Pt stream anomalies, in the centre of the KG1 body, do not correlate
348 with elevated Pt in the soils. Possibly, the streams locally record residual Pt enrichment
349 related to advanced weathering in a pronounced topographic gradient.

350 Of particular note are the high Pt/Pd ratios in the MdC (Pt/Pd mostly > 5), and the
351 lack of correlation between Pt and Pd (Fig. 11b). This pattern is in marked variance to
352 that observed in most other layered intrusions and mafic-ultramafic systems in general
353 (Fiorentini et al., 2012; Maier et al., 2013). In contrast, Pt shows well defined positive
354 correlations with the IPGE and Rh (Fig. 11a,c,d). Different blocks and sub-blocks of the
355 MdC define distinct correlations, with KG1 having a relatively Rh and a relatively Pt
356 enriched population, whereas KG1 extension, KG3 and KG4 each define distinct
357 populations.

358 Highly anomalous Pd values have been found in a single example of a sulfide-
359 bearing quartz vein associated with an amphibolite xenolith in drill core MPD 001
360 (Electronic Appendix 14). The rock contains up to 13.92 ppm Pd, 0.98% Cu, minor Au,
361 32 ppb Pt and < 10 ppb Rh and Ru.

362 The mantle normalized chalcophile element patterns for the orthopyroxenites and
363 norites from all intrusive blocks (Electronic Appendix 15) show a progressive increase
364 from Ir to Pt, followed by a decreasing trend through Pd and Au to Cu. The ophitic
365 gabbros show very different patterns, with a progressive increase from Ir to Cu, and a
366 small negative Au anomaly. The amphibolites have bowl-shaped patterns with strong
367 PGE depletion relative to Cu and Ni.

368 Ratio plots of Cu/Pd and Cu/Zr (Fig. 12) allow an estimate of the fertility of the
369 magmas. Cu/Pd of the orthopyroxenites and olivine pyroxenites is mostly around or
370 below the level of the primitive mantle (PM), with outliers possibly explained by Pd
371 mobility or localized and temporary sulfide saturation**.** Cu/Pd of the norites and gabbros
372 tends to be slightly above mantle (~11000), reflecting moderate Pd depletion of the
373 magma. The amphibolites have Cu/Pd significantly above mantle and thus crystallised
374 from a PGE depleted magma that equilibrated with sulfide prior to solidification. Cu/Zr
375 of most samples is 0.5-2, overlapping with, e.g., South African continental flood basalts
376 (Maier et al., 2003), consistent with crystallization of the MdC rocks from a S
377 undersaturated parent magma. Some samples have higher Cu/Zr. They could contain
378 small amounts of cumulus sulfide, consistent with their low Cu/Pd ratios. The PGE
379 depleted amphibolites have undepleted Cu/Zr suggesting that any sulfide that they
380 equilibrated with was of low volume.

381

382 **Sr and Nd isotopes**

383 Strontium isotope data of plagioclase from two orthopyroxenites, one olivine pyroxenite
384 and one gabbronorite from KG1 and KG3 show remarkable homogeneity between

385 samples as well as between intrusive blocks (Electronic Appendix 3 and 16). The samples
386 have $^{87}Sr/^{86}Sr_i$ 0.70255 - 0.70261 and positive εSr_T around +20, indicating an enriched
387 component.

388 The four samples analysed for whole rock Nd isotope ratios (Electronic Appendix
389 4) show εNd_T -0.6 to 0.3, i.e. little variation between samples and intrusive blocks. As in
390 the case of Sr isotopes, the Nd isotope data indicate the presence of an enriched
391 component. The ophitic gabbro (DY18) has εNd +1.8, suggesting magma derivation from
392 a depleted mantle source.

393

394 **X-RAY FLUORESCENCE MICROSCOPY**

395 X-ray fluorescence microscopy has provided added insight into the crystallization history
396 of the MdC rocks, allowing location and identification of trace Pt rich phases. Figures 13
397 and 14 show two orthopyroxenite heteradcumulates containing cumulus orthopyroxene,
398 approximately 5% plagioclase oikocrysts, minor intercumulus clinopyroxene, and trace
399 chromite and olivine inclusions within orthopyroxene.

400 More than a hundred small Pt-rich phases have been found in the five samples
401 mapped, with at least 12 in each sample, suggesting that such phases are quite common.
402 The elevated Pt content across significant core intervals, e.g., 200m with 50-100 ppb Pt in
403 drill core MPD 001 (Electronic Appendix 13) suggests a relatively homogenous
404 distribution of these phases, which in turn suggests that there are few large grains. Such
405 grains would be systematically under-sampled during petrographic analysis (Godel,
406 2013) and are unlikely to be detected by conventional methods.

The Pt phases located in the two samples reported in detail in this study are all less than 10 micrometres in size. The precise location in relation to the host grain boundary is difficult to determine precisely, owing to the unknown shape of the grain boundary in the third dimension, but it appears that all the Pt phases occur at or within a few tens of microns of the margins of orthopyroxene grains. Although the sample size is currently too small to be sure, none of the Pt phases was located within the Cr-zoned, chromite-bearing pyroxene grains, and their occurrence is apparently regardless of whether the host grain has a Ti-enriched rim. The great majority of grains so far identified fall at or close to the margins of orthopyroxene grains enclosed within plagioclase oikocrysts. This implies that the Pt phase or phases crystallised at the cumulus stage, but there is no association with chromite inclusions, as might have been predicted from the model of Finnigan et al. (2008).

The nature of the Pt-rich phases remains uncertain; all of the grains located so far lie beneath the surface of the host sample, and none have yet been observed optically or by SEM. Identification is therefore based on the element association obtained from the XFM data. About 50% of Pt grains show an association with As. For example, in sample Px21a there were 2 clusters of Pt grains, one associated with As, the other associated (but not co-located) with Ni and Cu. Approximate estimation of the depth of the grain in the sample in each case, based on variability of the apparent Pt peak height across the Maia detector array (Barnes et al., in preparation) indicates that in most cases Pt and As are co-located while the Ni-Cu peaks, attributed to sulfide phases, are slightly offset from Pt and As in 3D. The semi-quantified data indicate that in some, but not all, cases the visible coincident As and Pt spots on the map correspond approximately to sperrylite

stoichiometry, $PtAs_2$. It is likely that at least some of the Pt grains are sperrylite. However, Pd is not detected by this technique, and neither is Te, although Bi is detectable and none of the observed grains show any Bi association. Further investigation is ongoing to increase the sample size of detected grains, and to locate these phases.

The small sulphide grains associated in some cases with the Pt rich phases could have formed in response to reaction of the PGM with S-saturated trapped liquid, or S-bearing hydrous fluid, although there is no evidence for magmatic hydrous phases within these particular samples. The great majority of the 100+ grains so far identified are therefore attributable to direct magmatic precipitation of sperrylite and/or other Pt-dominant phases, thought most likely to be Pt-Fe alloys.

GEOCHRONOLOGY

Twelve analyses were taken from six baddeleyite grains (Electronic Appendix 17 and 18). The data scatter in $^{206}Pb/U$, and most are apparently discordant but this is presumed to be due to grain orientation effects. They are closely grouped in $^{207}Pb/^{206}Pb$, giving a weighted mean age of 2775 ± 11 Ma. However, there is some excess scatter (MSWD = 2.6). Low-side culling makes little difference to MSWD and high-side culling reduces it to <0.7, implying overculling. Given the modest size of the data set, the variable precision of the $^{207}Pb/^{206}Pb$ data and the lack of clear justification for any data rejection, we use the most conservative option, retaining all data and hence taking the age of baddeleyite crystallization to be 2775 ± 11 Ma.

Ten analyses were obtained from four monazite grains (Electronic Appendix 19 and 20). The majority of the results are apparently 5-6% discordant, however the

453 consistency of the offset from Concordia implies that this is due to a bias in Pb/U,
454 possibly due to an unidentified matrix effect. The variability of minor element contents
455 and lack of Y data make this impossible to assess, particularly for the one strongly
456 discordant point, which is from a very high-Th sample.

457 The data appear to fall into three categories. There are three points that are close
458 to Concordia and may be from concordant samples which have essentially identical
459 $^{207}Pb/^{206}Pb$. One other analysis matches this $^{207}Pb/^{206}Pb$ but is >10% discordant. This
460 analysis had low $CePO_2^+$ counts and very high Th contents, suggesting that the spot
461 inadvertently incorporated some huttonite. If this is true, the different (mixed) matrix
462 might explain the apparent discordance. It is also possible that huttonite is metamict and
463 has suffered "recent" Pb loss, and therefore that the analysed volume is genuinely
464 discordant. These four analyses come from four distinct sample grains. The weighted
465 mean $^{207}Pb/^{206}Pb$ dates for all four analyses is 2767 ± 7 Ma (including uncertainty
466 propagated from the $^{207}Pb/^{206}Pb$ reference sample PD-95 that was used for mass
467 fractionation correction), or 2766 ± 9 Ma if only the three most concordant analyses are
468 used. A fifth analysis is ~2σ from the main cluster; incorporating it into the weighted
469 mean gives 2765 ± 11 Ma, with only minor excess scatter (MSWD = 1.5).

470 The other data scatter along a trend that might be a mixing Discordia. The trend is too
471 short and Pb/U too susceptible to matrix-induced errors for a lower intercept to be
472 defined. However, it is almost inescapable to conclude that there has been at least one
473 younger episode of monazite growth or recrystallization. Therefore the monazite gives a
474 minimum age of 2765 ± 11 Ma for the orthopyroxenite, consistent with the baddeleyite
475 date.

476

477 **DISCUSSION**

478 **Parent magma composition**

479 The composition of the MdC parent magma remains difficult to constrain. We have used
480 two semi-quantitative approaches. First, we searched the literature to identify other
481 examples of orthopyroxenite cumulates of broadly similar composition to the MdC,
482 particularly those for which parent magma estimates are available. A relatively good
483 compositional overlap exists with Bushveld orthopyroxenites (Fig. 6, and Electronic
484 Appendix 11). We then simulated the crystallization of Bushveld B1 magma using PELE
485 (Boudreau, 1999). A particularly good fit with the MdC rocks is provided by sample
486 ECBV106 (Barnes et al., 2010: 10.07% MgO) at QFM and 100 bar. The simulation
487 yields spinel as the first mineral to crystallize followed by olivine (Fo85), orthopyroxene
488 (En86, after 10% crystallization) and then plagioclase (An69). Secondly, for one of our
489 best characterized and least evolved samples (Px21) we determined modal proportions by
490 point counting, and then subtracted the amount of MgO hosted by orthopyroxene from
491 the whole rock composition. This method gave 8% MgO for the intercumulus
492 component, but it needs to be borne in mind that the value is potentially affected by
493 residual liquid percolation.

494 To get a rough idea about the concentration of incompatible minor and trace
495 elements in the trapped melt, we have plotted best fit lines through the ultramafic rocks
496 (Electronic Appendix 21) and recorded the trace element concentration at 10% MgO
497 (TiO_2 0.4-0.5%, La ~8ppm, Ce ~10 ppm, Sm ~1-1.5 ppm, Th 2 ppm, Zr 40-60ppm, Ta
498 0.15 ppm, and Y 10-12ppm). Our data thus suggest that the MdC magma was a

magnesian basalt with approximately 10% MgO, relatively low TiO_2 contents around 0.5 wt%, yet relatively high concentrations of other incompatible trace elements. TiO_2/La ratios are comparable to continental flood-type basalts with similar MgO contents, e.g., Ventersdorp and Dominion (Marsh et al., 1989, 1992). The whole rock trace element data can be modeled by up to 20% combined assimilation-fractionation-contamination (AFC) of magnesian basalt (having trace element contents assumed to be 4x primitive mantle, i.e. equivalent to ~25% partial mantle melting) with a 17% partial melt of MdC country rock granite (average of samples GRA 2W and GRA 2X, Electronic Appendix 2). The composition of the granitic partial melt was calculated by assuming restite modal proportions determined in melting experiments of biotite gneiss at 875° and 3kbar (Patino Douce and Beard, 1995), and D values summarized in Rollinson (2013) (Fig. 15). However, as the model contains a large number of variables, other interpretations are possible, including a magma source in the metasomatised mantle.

The Nd and Sr isotope data are broadly consistent with the interpretations from the trace element data. Assuming that the host granites had Sr_i of 0.7013 at 3120±67Ma (Rb/Sr whole rock method, Caen Vachette et al., 1988), and εNd 0.2 (i.e., approximately $CHUR_T$), and that the MdC magma was a magnesian basalt with 4x PM levels of Rb, Sr, Sm and Nd (Sun and McDonough, 1989), Sr_i 0.701, and εNd 2,1 (DM, De Paolo 1981), the MdC samples (Sr_i 0.70255-0.70261, εNd 0.3 to -0.6) can be modeled by 10-15% bulk contamination with host granite. Unfortunately, Caen Vachette et al. (1988) do not provide detailed information on sampling sites or trace element geochemistry, and their Rb-Sr dates have large uncertainties, which renders the above modeling semi-quantitative

521 at best. To improve the reliability of the model, high-precision geochronology, isotope
522 geochemistry and trace element data of the host granites are required.

523 The two ophitic gabbroic samples cannot represent the parent magma to the
524 orthopyroxenites and norites, as the gabbros have distinctly less fractionated trace
525 element patterns and less enriched Nd isotope signatures, as well as depleted PGE
526 contents (Cu/Pd >7000). Whether the gabbros do indeed belong to the same magmatic
527 event as the remainder of the MdC cumulates needs to be confirmed by dating.

528

529 **Nature of PGE enrichment and PGE host phases**

530 The Pd levels of most MdC ultramafic samples can be modeled by assuming that the
531 rocks contain 10-30% trapped liquid (broadly consistent with petrography) with 20-25
532 ppb Pd. Such levels are at the upper end of Pd contents in global basalts (Fiorentini et al.,
533 2010; Maier et al., 2013). Other examples of Pd rich basalts include Finnish 2.45 Ga
534 tholeiitic dykes having up to 30-35 ppb (Guo et al., 2012), and Svecofennian basalts
535 reaching 25 ppb (Barnes et al., 2009).

536 In contrast to Pd, the measured Pt contents of the MdC cumulates are far too high
537 to be explained by a trapped liquid component. Our global database indicates that basaltic
538 magmas may contain up to ~20 ppb Pt (Maier et al., 2013). A 30% trapped liquid
539 component could thus account for no more than 6-7 ppb Pt. Hydrothermal introduction of
540 Pt or removal of Pd and S after crystallization is considered unlikely, in view of the
541 relatively homogenous nature of the PGE contents in the MdC along ~100km strike, and
542 the generally unaltered nature of the rocks. Localized mobility of Pd is indicated by the

543 development of vein-style mineralization, but this is extremely rare and closely
544 associated with amphibolite xenoliths.

545 A more likely scenario is that the MdC magma had Pt contents in the range of
546 other basalts (15-20 ppb), but reached Pt (or $PtAs_2$) saturation prior to sulfide saturation.
547 This model is consistent with the synchrotron XFM data reported above and the low S
548 contents of the MdC rocks (Fig. 7). Compatible behavior of Pt has previously been
549 reported from other basaltic suites, including the Pual ridge (Park et al., 2012), where it
550 was assigned to precipitation of Pt alloys.

551 As platinum shows well defined positive correlations with Ir, and to a lesser
552 extent Ru and Rh (Fig. 11), these metals also appear to have been compatible during
553 fractionation. Compatibility of IPGE in mafic-ultramafic rocks has been described in
554 many igneous suites (Barnes et al., 1985, Puchtel and Humayun, 2001). From a crystal-
555 chemical point of view, the IPGEs could be hosted by orthopyroxene and olivine,
556 substituted for Mg in octahedral coordination, which has been shown to be the case for
557 Ru, Rh and Ir in olivine (Brenan et al., 2003; 2005). Several studies have proposed that
558 in mafic-ultramafic rocks the IPGE are mainly hosted by Os-Ir-Ru alloys and PGM (e.g.,
559 Peck and Keays, 1990), but as yet no IPGE enriched PGM could be identified in the
560 MdC. Another possible host for the IPGE is chromite (Locmelis et al., 2011; Pagé et al.,
561 2012), but chromite is rare in the MdC and thus unlikely to control IPGE distributions, at
562 least in the form of solid solution. Some of the IPGE and Rh could be hosted in Pt alloys.
563 For example, Pt alloys described by Garuti et al. (2002) have approximately 80% Pt, and
564 1-2% Ir, Ru, and Rh. However, in the MdC we do not see any detectable IPGE associated
565 with the As phases, or anywhere else.

Factors controlling Pt saturation

PGE levels in basaltic magmas depend largely on the solubility of sulfide liquid, platinum-group minerals and PGE alloy during mantle melting and fractional crystallization in the crust. Small to medium degree (<10-20%) melts of asthenospheric mantle are saturated in sulfide (Barnes et al., 1985; Rehkämper et al., 1999; Mungall and Brenan, 2014) and thus depleted in all PGE. Upon dissolution of the mantle sulfides at larger degrees of melting, the concentrations of the individual PGE in the magma depend on whether sulfide is the main PGE host phase or whether, in addition, any PGM or PGE alloy is stable. Palladium is only controlled by sulfide and thus large degree mantle melts such as komatiites have Pd levels 2-3 times that of the primitive mantle (Fiorentini et al., 2013). Platinum levels additionally depend on whether Pt alloy is stable, which in turn is controlled by T, fO_2 and depth of melting (Mungall and Brenan, 2014). At relatively low pressure, Pt alloy is stable even at large degree melting, resulting in sub-chondritic Pt/Pd ratios in most asthenospheric mantle magmas (e.g., MORB and komatiites). Increased temperature, fO_2 and melting depth enhance Pt alloy solubility (Borisov and Palme, 1997; Fortenfant et al., 2003; Mungall and Brenan, 2014) leading to a decrease in the bulk partition coefficient of Pt. This should result in relatively high Pt/Pd in the melt, perhaps approaching the chondritic ratio as observed in Bushveld magmas. However, it is notable that global mantle melts mostly show Pt contents between 10-15 ppb (Maier et al., 2009; Fiorentini et al., 2010), with very few examples of higher values that might be expected in large degree melts generated at high pressure. This is likely due to the fact that the Pt

588 levels of the magmas are capped by decreasing Pt solubility during magma ascent
589 resulting in the precipitation of Pt alloys or PGM.

590 Enigmatically, the empirical data indicate much higher Pt solubilities in mafic
591 magmas (10-15 ppb) than the available experimental data. Thus, Ertel et al. (1999) show
592 that Pt solubility in basalt is as low as 3 ppb. Borisov and Palme (1997) proposed higher
593 values, around 15 ppb, but their experiments probably overestimate the Pt solubility, as
594 that work involved bulk analyses in which samples may have been contaminated with
595 undissolved Pt particles. The mismatch between the natural magmas and the experimental
596 data suggests that either the solubility model is wrong, or that other factors play a role.
597 The experiments of Ertel et al. (1999) and Borisov and Palme (1997) were conducted on
598 synthetic basalts which contained no Fe or S. Fe addition should result in the formation of
599 Pt alloys and thus relatively lower Pt solubility (Borisov and Palme, 2000). However,
600 Laurenz et al. (2013) have shown that the presence of sulfur in magmas significantly
601 increases Pd and Ru solubility, and Mungall and Brenan (2014) have suggested a similar
602 effect on Pt.

603 Of particular interest is the origin of the Pt enriched layer of the MdC (Fig. 10,
604 and Electronic Appendix 13). The Pt rich samples are heteradcumulates that largely lack
605 chromite and olivine. They have the highest Mg#, i.e., are the least evolved, but in terms
606 of petrography, isotopes and incompatible trace element ratios they are compositionally
607 indistinguishable from the other rocks. Due to the small size of the Pt phases located,
608 gravitational concentration from convecting magma seems unlikely, unless the Pt phases
609 nucleated on the surface of cumulus orthopyroxene grains and were mechanically
610 concentrated with them. The Pt solubility could have been temporarily lowered due to

611 reduction of the magma in response to contamination, but not only would this potentially
612 have triggered sulfide saturation (Tomkins et al., 2012), but it is also inconsistent with the
613 V contents of the rocks; The experimental data of Toplis and Corgne (1992) have shown
614 that partitioning of V into pyroxene increases with falling O fugacity. Thus, one would
615 expect an increase in V to accompany the Pt enrichment, contrary to the observations
616 from the drillcore data that show inflections towards low V contents in the Pt rich layer.
617 Furthermore, there is no lithological evidence such as country rock xenoliths that could
618 suggest local magma contamination in the Pt enriched horizon. Localised reduction due
619 to chromite crystallization (Finnigan et al., 2008) can be ruled out because the most Pt
620 rich samples are chromite poor, and no Pt phases were observed by XFM mapping in
621 contact with chromite grains. The available evidence suggests that the formation of the Pt
622 enriched layer is related to magma replenishment with relatively unevolved magma,
623 consistent with a subtle increase in Mg# and a decrease in V and Ti of the rocks.
624 An additional factor suggested by our observations is that arsenic plays a role in
625 the stability of magmatic Pt phases. The evidence for primary precipitation of Pt-As rich
626 phases, thought to be sperrylite, suggest that the key factor may be the magma exceeding
627 the solubility product for sperrylite. If Pt is dissolved in the magma as PtS, as implied by
628 the experimental data of Mungall and Brenan (2014), then the following reaction may be
629 operating:
630 $PtS(melt) + FeAs_2(melt) = PtAs_2(solid) + FeS(melt)$
631 with the reaction being driven by the increasing activity coefficient of PtS with
632 falling temperature along a given fO_2 buffer implied by the Mungall and Brenan
633 experiments. This conjecture requires testing by investigation of solution properties of Pt

634 in the presence of As in silicate melts, which are currently unknown. The divergence of
635 Pt/Pd ratio noted in a number of layered intrusions and mafic lava suites (e.g., Stillwater,
636 Keays et al., 2012; Deccan Trap lavas, Keays and Lightfoot, 2010) may be explained by
637 preferential fractionation of magmatic Pt arsenides.

638 Unfortunately, no arsenic data are available to evaluate whether the elevated Pt
639 contents in the MdC rocks could be due to unusually high As concentrations in the
640 magma. However, assuming that all of the Pt occurs as $PtAs_2$, with overall Pt levels at
641 ~20-150 ppb, this would require ~15-100 ppb As for charge balance. This is in the range
642 of As contents reported by Jenner and O'Neill (2012) for MORB in the 8-10 wt% MgO
643 range (~125 ppb As). Hence, the required As contents implied by the Pt contents of the
644 rocks are not exceptional, adding support to the notion that Pt-arsenide might be more
645 significant in S-poor rocks than previously supposed (J Brenan, written comment, Feb.
646 2015).

647

648 **CONCLUSIONS**

649 The Monts de Cristal Complex of Gabon forms a large layered intrusion, approximately
650 100km long and 1-3 km wide. It consists predominantly of orthopyroxenite that
651 crystallised from a low-Ti basalt with approximately 10% MgO. The Complex is
652 characterised by strong enrichment in Pt (up to 150 ppb) relative to Pd (<20 ppb) and
653 other chalcophile elements and sulphur. X-Ray fluorescence microscopy has identified
654 numerous small (<10 micrometers) Pt rich phases, mostly arsenides. This is interpreted to
655 indicate precipitation of Pt-arsenides from S undersaturated magma, constituting some of

656 the best evidence yet for direct crystallization of platinum- group minerals from basaltic
657 magma.
658
659 **ACKNOWLEDGEMENTS**
660 We thank Sari Forss for producing thin sections, Leena Järvinen and Arto Pulkkinen for
661 assistance with Sm-Nd isotope analysis, and Chris Ryan, Martin de Jonge and Daryl
662 Howard for assistance and support in the XFM mapping component of this research,
663 which was undertaken on the X-Ray Fluorescence Microscopy (XFM) beamline at the
664 Australian Synchrotron, Victoria, Australia (AS grant 6618 to Godel, Barnes and Maier).
665 C Li and J-W Park engaged in helpful discussions on S and Pt saturation. Lonmin is
666 thanked for granting permission to publish the findings of our research and the
667 geochemical data on the drill cores. Martin Prendergast allowed the use of his field map
668 in Fig. 2. Discussions with Sarah-Jane Barnes and constructive reviews by Chusi Li and
669 James Brenan helped to improve the manuscript significantly. This is an output from the
670 CSIRO Minerals Down Under National Research Flagship.
671
672
673 **REFERENCES**
674 Arsandaux, H. (1912). Sur la presence au Gabon de roches appartenant a la serie de la
675 charnockite. *Comptes Rendus Academie Sciences*, Paris, **154**, 896-898.
676
677 Aubague. M. & Hausknecht, J.J. (1959). *Carte geologique de reconnaissance au l/500*
678 *000, feuille Libreville Est. Carte et notice explicative*. Direction des Mines et de la
679 Geologie de I'AEF, Brazzaville, Congo, 34p.
680

681 Ballhaus, C., Berry, R.F. & Green, D.H. (1991). High pressure experimental calibration
682 of the olivine-orthopyroxene-spinel oxygen geobarometer: implications for the oxidation
683 state of the upper mantle. *Contributions to Mineralogy and Petrology* **107**, pp 27-40
684
685 Barnes, Sarah-Jane & Maier, W.D. (1999). *The fractionation of Ni, Cu and the noble*
686 *metals in silicate and sulphide liquids*, in Keays, R.R., Lesher, C.M., Lightfoot, P.C. and
687 Farrow, C.E.G., eds., *Dynamic processes in magmatic ore deposits and their application*
688 *to mineral exploration*: Geological Association Canada, Short Course Notes, **13**, 69-106.
689
690 Barnes, Sarah-Jane, Naldrett, A.J. & Gorton, M.P. (1985). The origin of the fractionation
691 of platinum-group elements in terrestrial magmas. *Chemical Geology* **53**, 303-323.
692
693 Barnes, Sarah-Jane, Maier, W.D. & Curl, E.A. (2010). Composition of the Marginal
694 rocks aand sills of the Rustenburg layered suite, Bushveld Complex, South Africa:
695 Implications for the formation of platinum-group element deposits. *Economic Geology*
696 **105**, 1491-1511.
697
698 Barnes, S.J. (2007). Cotectic precipitation of olivine and sulfide liquid from komatiite
699 magma and the origin of komatiite-hosted disseminated nickel sulfide mineralization at
700 Mount Keith and Yakabindie, Western Australia. *Economic Geology* **106**, 298-304.
701
702 Barnes, S.J. & Naldrett A.J. (1984). Geochemistry of the J-M Reef of the Stillwater
703 Complex, Minneapolis Adit area II. Slicate Mineral Chemistry and Petrogenesis. *Journal*
704 *of Petrology*, **27**, 791-825.
705
706 Barnes, S.J., Makkonen, H.V., Dowling, S.E., Hill, R.E.T. & Peltonen, P. (2009). The
707 1.88 Ga Kotalahti and Vammala nickel belts, Finland: geochemistry of the mafic and
708 ultramafic metavolcanic rocks. *Bulletin of the Geological Society of Finland* **81**, 103–
709 141.
710

711 Barnes, S.J., Osborne, G.A., Cook, D., Barnes, L., Maier, W.D. & Godel, B. (2011), The
712 Santa Rita Nickel sulfide deposit in the Fazenda Mirabela Intrusion, Bahia, Brazil:
713 Geology, sulfide geochemistry and genesis. *Economic Geology* **106**, 1083-1110.
714
715 Barnes, S. J., Van Kranendonk, M. J., and Sonntag, I., 2012, Geochemistry and tectonic
716 setting of basalts from the Eastern Goldfields Superterrane: *Australian Journal of Earth*
717 *Sciences* **59**, 707-735.
718
719 Borisov, A. & Palme, H. (1997), Experimental determination of the solubility of
720 platinum in silicate melts. *Geochimica et Cosmochimica Acta* **20**, 4349-4357.
721
722 Borisov A., Palme H. (2000) Solubilities of noble metals in Fe-containing silicate melts
723 as derived from experiments in Fe-free system. American Mineralogist. 85 (11-12), pp.
724 1665-1673
725
726 Boudreau, A.E. (1999), PELE-a version of the MELTS software programme for the PC
727 platform. *Computers and Geosciences* **25**, 201-203.
728
729 Bowles, J.F.W., Prichard, H.M., Suarez, S. & Fisher, P.C. (2013). The first report of
730 PGM in magnetite-bearing gabbro, Freetown layered complex, Sierra Leone:
731 Occurrences and genesis. *Canadian Mineralogist* **51**, 455-473.
732
733 Brenan J. M., McDonough W. F. and Dalpe´ C. (2003) Experimental constraints on the
734 partitioning of rhenium and some platinum-group elements between olivine and silicate
735 melt. *Earth Planet. Sci. Lett*. **212**, 135–150.
736
737 Brenan J. M., McDonough W. F. and Ash R. (2005) An experimental study of the
738 solubility and partitioning of iridium, osmium and gold between olivine and silicate melt.
739 *Earth Planet. Sci. Lett*. **237**, 855–872.
740

741 Caen-Vachette, M., Vialette, Y., Basset, J.P. & Vidal, P. (1988). Apport de la
742 geochronologie isotopique a la connaissance de la geologic gabonaise. *Chronique*
743 *Recherche Miniere* **491**, 35-53.
744
745 Campbell, I. H. & Griffiths, R. W. (1992). The changing nature of mantle hotspots
746 through time: implications for the chemical evolution of the mantle. *Journal of Geology*
747 **92**, 497-523.
748
749 Campiglio, C. (1987). *Perspectives sur la recherche de platinoides dans le complexe des*
750 *Monts de Cristal, Gabon*. In: Rapport d'Execution de la Convention Concernant la
751 Cellule d'orientation de I'lnventaire Minier Gabonais, 1986-1987. Armines-CGGM,
752 France, 31-36.
753
754 Campiglio, C., Marion, C. & Vannier, M. (1983). *Le complexe mafique-ultramafique de*
755 *M'Bilan. Etude des premiers echantillons de roches et de concentres alluvionnaires*. In:
756 Annexes, Rapport Cellule d'orientation de I'lnventaire Minier, CGGM. Direction des
757 Mines et de la Geologie Miniere, Libreville, Gabon, 22p.
758
759 Chevalier, L., Makanga, J.F. & Thomas, R.J. (2002). *Carte geologique de la Republique*
760 *Gabonaise. Notice explicative*. Council for Geoscience, Pretoria, 195p.
761
762 Creighton, S., Stachel, T., Eichenberg, D. & Luth, R.W. (2010). Oxidation state of the
763 lithospheric mantle beneath Diavik diamond mine, central Slave craton, NWT, Canada.
764 *Contributions to Mineralogy and Petrology* **159**, 645-657.
765
766 DePaolo, D.J. (1981). Neodymium isotopes in the Colorado Front Range and
767 crust-mantle evolution in the Proterozoic. *Nature* **291**, 684–687.
768
769 Edou-Minko, A., Grandin, G. & Campiglio, C. (2002). Petrologie et geomorphologie
770 dans la region de Kango, Gabon: un grand dyke ultramafique-mafique archeen. *Journal*
771 *of African Earth Sciences* **32**, 899-918.

Ertel W., O'Neill H., St C., Sylvester P. J. and Dingwell D. B. (1999) Solubilities of Pt and Rh in a haplobasaltic melt at 1300 °C. *Geochim. Cosmochim. Acta* **63**, 2439–2449.

Finnigan, C.S., Brenan, J.M., Mungall, J.E. & McDonough, W.F. (2008). Experiments and Models Bearing on the Role of Chromite as a Collector of Platinum Group Minerals by Local Reduction. *Journal of Petrology* **49**, 1647-1665.

Fiorentini ML, Barnes SJ, Lesher CM, Heggie, GJ, Keays RR, Burnham OM (2010) Platinum Group Element Geochemistry of Mineralized and nonmineralized Komatiites and Basalts. *Economic Geology*, **105**, 795-823.

Fiorentini, M.L., Barnes, S.J., Maier, W.D. & Heggie, G.J. (2012). Global variability in the PGE contents of komatiites, *Journal of Petrology* **52**, 82-112.

Fletcher, I.R., McNaughton, N.J., Davis, W.J., Rasmussen, B., 2010. Matrix effects and calibration limitations in ion probe U–Pb and Th–Pb dating of monazite. *Chemical Geology* **270**, 31–44.

Fortenfant, S.S., Gunther, D., Dingwell, D.B. & Rubie, D.C. (2003). Temperature dependence of Pt and Rh solubilities in a haplobasaltic melt. *Geochimica et Cosmochimica Acta* **67**, 123-131.

Garuti, G., Pushkarev, E.V. & Zaccarini, F. (2002). Composition and paragenesis of Pt alloys from chromitites of the Uralian-Alaskan-type Kytlym and Uktus complexes, northern and central Urals, Russia. *Canadian Mineralogist* **40**, 1127-1146.

Godel , B. (2013). High-Resolution X-Ray Computed Tomography and Its Application to Ore Deposits: From Data Acquisition to Quantitative Three-Dimensional Measurements with Case Studies from Ni-Cu-PGE Deposits. *Economic Geology* **108**, 2005-2019.

Harris, C., Pronost, J.J.M., Ashwal, L.D. & Cawthorn, R.G. (2004). Oxygen and hydrogen isotope stratigraphy of the Rustenburg layered suite, Bushveld Complex: constraints on crustal contamination. *Journal of Petrology* **46,** 579–601.

Huhma, H., Kontinen, A., Mikkola, P., halkoaho, T., Hokkanen, T., Hölttä, P., Juopperi, H., Konnunaho, J., Luukkonen, E., Mutanen, T., Peltonen, P., Pietikäinen, K., Pulkkinen, A., 2012. Sm–Nd results on the Archean crust in Finland. In: Hölttä, P. (Ed.), *The Archean of the Karelia Province in Finland*. Geological Survey of Finland, Special Paper 54, pp. 176–213.

Irvine, T.N. (1970). *Crystallization sequences in magmas of the Muskox intrusion and some other layered intrusions*. Geological Society of South Africa, Special Publication **1**, 441-476.

Irvine, T.N. (1980). *Magmatic infiltration metasomatism, double-diffusive fractional crystallisation, and adcumulus growth in the Muskox Intrusion and other layered intrusions*. In: R.B. Hargraves (Editor), Physics of Magmatic Processes. Princeton University Press, Princeton, N.J., 325-383.

Jacobsen, S.B. & Wasserburg, G.J. (1980). Sm-Nd isotopic evolution of chondrites. *Earth and Planetary Science Letters* **50**, 139–155.

Kassa-Mombo, C., Minko-Bidza, V., Mikhailoff, N., Greenish, T., Devos, W., Boldrachi, R., Degroote, V., Bonnot, H., Adlof, L., Mabiala, R., Melchior, A. & Abeme, M.J. (1988). Apport de I'inventaire aux connaissances geologiques et minieres des feuilles a l/200.000 de Libreville, Kango et Lambarene (Gabon). *Chronique Recherche Miniere* **491**, 105-124.

Keays, R.R., Lightfoot, 2010. Crustal sulfur is required to form magmatic Ni-Cu sulfide deposits; evidence from chalcophile element signatures of Siberian and Deccan Trap basalts. *Mineralium Deposita*, **45**, 241.

Keays, R.R., Lightfoot, P.C., Hamlyn, P.R., 2012. Sulfide saturation history of the Stillwater Complex, Montana: chemostratigraphic variation in platinum group elements. *Mineralium Deposita,* **47**, 151-173.

Kirkham, R., Dunn, P. A., Kucziewski, A., Siddons, D. P., Dodanwela, R., Moorhead, G., Ryan, C. G., De Geronimo, G., Beuttenmuller, R., Pinelli, D., Pfeffer, M., Davey, P., Jensen, M., Paterson, D., de Jonge, M. D., Kusel, M. & McKinlay, J. (2010). *The Maia Spectroscopy Detector System: Engineering for Integrated Pulse Capture, Low-Latency Scanning and Real-Time Processing*. AIP Conference Series, **1234**, 240-243.

Laurenz V, Fonseca ROC, Ballhaus C, Jochum KP, Heuser A, Sylvester PJ (2013) The solubility of palladium and ruthenium in picritic melts: 2. The effect of sulfur. *Geochim. Cosmochim. Acta*, **108**, 172-183

Li, C. & Ripley, E.M. (2009). Sulphur contents at sulfide-liquid or anhydrite saturation in silicate melts: empirical equations and example applications. *Economic Geology* **104**, 405-412.

Lightfoot, P.C. & Naldrett, A.J. (1983). The geology of the Tabankulu section of the Insizwa Complex, Transkei, southern Africa, with reference to the nickel sulphide potential. *Transactions of the Geological Society of South Africa*, **86**, 69–187.

Lightfoot, P.C., Naldrett, A.J. & Hawkesworth, C.J. (1984). The geology and geochemistry of the Waterfall Gorge Section of the Insizwa Complex with particular reference to the origin of the nickel sulphide deposits. *Economic Geology*, **79**, 1857–1879.

Locmelis, M., Pearson, N.J., Barnes, S.J. & Fiorentini, M.I. (2011). Ruthenium in komatiitic chromite. *Geochimica et Cosmochimica Acta* **75**, 3645-3661.

Ludwig, K.R. (2003). *User's Manual for Isoplot/Ex version 3.00–A Geochronology Toolkit for Microsoft Excel, No. 4* - Berkeley Geochronological Center, Special Publication

Maier WD (2004). Monts de Cristal PGE project. Internal Report 2, SouthernEra Resources Ltd.

Maier WD (2009). Report on PGE reef potential of the Monts de Cristal PGE project, Gabon, Lonmin Plc

Maier, W.D. & Eales, H.V. (1997). *Correlation within the UG2–Merensky Reef interval of the Western Bushveld Complex, based on geochemical, mineralogical and petrological data*. Geological Survey of South Africa Bulletin **120**, 56 p.

Maier, W.D., Groves, D.I. (2012). Temporal and spatial controls on the formation of magmatic PGE and Ni-Cu deposits. *Mineralium Deposita* **46**, 841-857.

Maier, W.D., Barnes, S.-J. & Marsh, J.S. (2003). The concentrations of the noble metals in Southern African flood-type basalts and MORB: implications for petrogenesis and sulphide exploration. *Contributions to Mineralogy and Petrology* **146**, 44-61.

Maier, W.D., Gomwe, T., Barnes, S.-J., Li, C. & Theart, H. (2004). Platinum-group elements in the Uitkomst Complex, South Africa. *Economic Geology* **99**, 499-516.

Maier, W.D., Barnes, S.-J. & Groves, D.I. (2013). The Bushveld Complex, South Africa: formation of platinum– palladium, chrome- and vanadium-rich layers via hydrodynamic sorting of a mobilized cumulate slurry in a large, relatively slowly cooling, subsiding magma chamber. *Mineralium Deposita* **48**, 1–56.

895 Marsh JS, Bowen MP, Rogers NW, Bowen TB (1989) Volcanic rocks of the
896 Witwatersrand Triad, South Africa, I: Petrogenesis of mafic and felsic rocks of the
897 Dominion Group. *Precambrian Research* 44, 39–65
898
899 Marsh JS, Bowen MP, Rogers NW, Bowen TB (1992) Petrogenesis of Late Archean
900 flood-type basic lavas from the Klipriviersberg group, Ventersdorp Supergroup, South
901 Africa. *Journal of Petrology* **33**, 817– 847
902
903 Martin, H., Smithies, R.H., Rapp, R., Moyen, J.-F. & Champion, O. (2005). An overview
904 of adakite, tonalite–trondhjemite–granodiorite (TTG), and sanukitoid: relationships and
905 some implications for crustal evolution. *Lithos* **79**, 1–24.
906
907 Mavrogenes, J. A. & O'Neill, H.St.C. (1999). The relative effects of pressure,
908 temperature and oxygen fugacity on the solubility of sulfide in mafic magmas.
909 *Geochimica et Cosmochimica Acta* **63**, 1173–1180.
910
911 McDonald, I. & Viljoen, K.S. (2006). Platinum-group elemeent geochemistry of mantle
912 eclogites: a reconnaissance study of xenoliths from the Orapa kimberlite, Botswana.
913 *Transactions Institution Mining and Metallurgy* **115**, 81-93.
914
915 McDonough, W.F. & Sun, S.-s. (1995). The composition of the Earth. *Chemical Geology*
916 **120**, 223-253.
917
918 McInnes, B.I.A., McBride, J.S., Evans, N.J., Lambert, D.D. & Andrew, A.S. (1999).
919 Osmium isotope constraints on metal recycling in subduction zones. *Science* **286**, 512-
920 516.
921
922 Merkle, R.K.W. (1992). Platinum-group minerals in the middle group of chromitite
923 layers at Marikana, western Bushveld Complex: indications for collection mechanisms
924 and postmagmatic modification. *Canadian Journal of Earth Sciences* **29**, 209-221.
925

926 Müller, W., Shelley, M., Miller, P. & Broude, S. (2009). Initial performance metrics of a
927 new custom-designed ArF excimer LA-ICPMS system coupled to a two-volume laser-
928 ablation cell. *Journal Anal Atom Spectrom* **24,** 209–214.
929
930 Mungall, J.E. & Brenan, J.M. (2014). Partitioning of platinum-group elements and Au
931 between sulfide liquid and basalt and the origins of mantle-crust fractionation of the
932 chalcophile elements. *Geochimica et Cosmochimica Acta* **125**, 265–289.
933
934 Nebel, O., Scherer, E.E. & Mezger, K. (2011). Evaluation of the ^{87}Rb decay constant by
935 age comparison against the U–Pb system. *Earth and Planetary Science Letters* **301,** 1–8.
936
937 Pagé, P., Barnes, S.-J., Bédard, J.H. & Zientek, M.L. (2012). In situ determination of Os,
938 Ir, and Ru in chromites formed from komatiite, tholeiite and boninite magmas:
939 implications for chromite control of Os, Ir and Ru during partial melting and crystal
940 fractionation. *Chemical Geology* **302–303,** 3–15.
941
942 Park, J.-W., Campbell, I.H. & Arculus, R.J. (2013). Platinum-alloy and sulfur saturation
943 in an arc-related basalt to rhyolite suite: Evidence from the Pual Ridge, eastern Manus
944 Basin. *Geochimica et Cosmochimica Acta* **101**, 76–95.
945
946 Paterson, D., de Jonge, M. D., Howard, D. L., Lewis, W., McKinlay, J., Starritt, A.,
947 Kusel, M., Ryan, C. G., Kirkham, R., Moorhead, G. & Siddons, D. P. (2011). *The X-ray*
948 *Flurorescence Microscopy Beamline at the Australian Synchroton*. AIP Conference
949 Proceedings, **1365**, 219-222.
950
951 Patino Douce, A.E. & Beard, J.S. (1995). Dehydration-melting of Biotite Gneiss and
952 Quartz Amphibolite from 3 to 15 kbar. *Journal of Petrology* **36**, 707-738.
953
954 Peck D. C., Keays R. R. & Ford R. J. (1992). Direct crystallization of refractory
955 platinum-group element alloys from boninitic magmas: evidence from western Tasmania.
956 *Australian Journal of Earth Sciences* **39**, 373–387.

Prendergast, M. (2009). *Monts de Cristal Platinum Project, NW Gabon*. Geological report on exploration activities. Lonmin plc.

Puchtel, I.S. and Humayun, M. (2001) Platinum group element fractionation in a komatiitic basalt lava lake. Geochim. Cosmochim. Acta 65: 2979-2994.

Raedeke, L.D. (1982). *Petrogenesis of the Stillwater Complex*. Unpublished PhD thesis, University of Washington, Seattle, 212p.

Rankenburg, K., Lassiter, J.C. & Brey, G. (2004). Origin of megacrysts in volcanic rocks of the Cameroon volcanic chain – constraints on magma genesis and crustal contamination. *Contributions to Mineralogy and Petrology* **147**, 129-144.

Rehkamper, M., Halliday, A.N., Fitton, J.G., Lee, D.-C., Wieneke, M., & Arndt, N.T. (1999). Ir, Ru, Pt and Pd in basalts and komatiites: New constraints for the geochemical behavior of the platinum group elements in the mantle. Geochimica et Cosmochimica Acta 63, 3915-3934.

Richard, P., Shimizu, N. & Allègre, C.J. (1976). 143Nd/146Nd, a natural tracer: an application to oceanic basalts, *Earth and Planetary Science Letters* **31**, 269–278.

Rollinson HR (2013) Using geochemical data: evaluation, presentation, interpretation, Routledge, Oxon, UK.

Rudnick, R.L. & Fountain, D.M. (1995). Nature and composition of the continental crust: A lower crustal perspective. *Reviews in Geophysics* **33**, 267–309.

Ryan, C., Kirkham, R., Hough, R., Moorhead, G., Siddons, D., de Jonge, M., Paterson, D., De Geronimo, G., Howard, D. & Cleverley, J. (2010a), Elemental X-ray imaging using the Maia detector array: The benefits and challenges of large solid-angle: *Nuclear*

Instruments & Methods in Physics Research, Section A–Accelerators, Spectrometers, Detectors and Associated Equipment **619**, 37-43.

Ryan, C., Kirkham, R., Siddons, D., Dunn, P., Laird, J., Kuczewski, A., Moorhead, G., De Geronimo, G., Davey, P., Jensen, M., Paterson, D., de Jonge, M., Howard, D. & Hough, R. (2010b). The Maia 384 detector array in a nuclear microprobe: A platform for high definition PIXE elemental imaging: *Nuclear Instruments & Methods in Physics* Research Section B-Beam Interactions with Materials and Atoms **268**, 1899-1902.

Ryan, C. G. (2000). Quantitative Trace Element Imaging using PIXE and the Nuclear Microprobe. *International Journal of Imaging Systems and Technology* **11**, 219-230.

Ryan, C.G., Siddons, D.P., Kirkham, R., Li, Z.Y., de Jonge, M.D., Paterson, D.J., Cleverley, J.S., Kuczewski, A., Dunn, P.A., Jensen, M., De Geronimo, G., Howard, D.L., Godel, B., Dyl, K.A., Fisher, L.A., Hough, R.M., Barnes, S.J., Bland, P.A., Moorhead, G.F., James, S.A., Spiers, K.M., Falkenberg, G., U , Boesenberg, U., Wellenreuther, G., (2014). The Maia detector array and x-ray fluorescence imaging system: locating rare precious metal phases in complex samples Proc. SPIE 8851, X-Ray Nanoimaging: Instruments and Methods 8851, 88510Q.

Ryan, C. G., Siddons, D. P., Kirkham, R., Dunn, P. A., Kuczewski, A., Moorhead, G., De Geronimo, G., Paterson, D. J., de Jonge, M. D., Hough, R. M., Lintern, M. J., Hoard, D. L., Kappen, P. & Cleverley, J. (2010c). The New Maia Detector System: *Methods for High Definition Trace Element Imaging of Natural Material*, in Denecke, M. A., and Walker, C. T., eds., *X-Ray Optics and Microanalysis*, **1221**, 9-17.

Sobolev S.V., Sobolev, A.V., Kuzmin D.V., Krivolutskaya, N.A., Petrunin, A.G., Arndt, N.T., Radko, V.A., & Vasiliev, Y.R. (2011). Linking mantle plumes, large igneous provinces and environmental catastrophes. *Nature* **477**, 312-316.

1017 Teigler, B. & Eales, H.V. (1996). *The lower and critical zones of the western limb of the*
1018 *Bushveld Complex, as indicated by the Nooitgedacht boreholes*. Geological Survey of
1019 South Africa Bulletin **111**, 126
1020
1021 Thompson, R.N. Morison, M.A., Dicken, A.P. & Hendry, G.L. (1983). *Continental flood*
1022 *basalts ... Archahnids rule OK?* In: Hawkesworth, C.J. and Norry, M.J. (eds.) *Continental*
1023 *basalts and mantle xenoliths*. Shiva Nantwich, 158-185.
1024
1025 Tomkins, A.G., Rebryna, K.C., Weinberg, R.F. & Schaefer, B.F. (2012). Magmatic
1026 Sulfide Formation by Reduction of Oxidized Arc Basalt. J Petrol., 53, 1537-1567.
1027
1028 Toplis, M.J. & Corgne, A. (2002). An experimental study of element partitioning
1029 between magnetite, clinopyroxene and iron-bearing silicate liquids with particular
1030 emphasis on vanadium. *Contributions to Mineralogy and Petrology* **144,** 22–37.
1031
1032 Wille, M., Kramers, J.D., Nägler, T.F., Beukes, N.J., Schröder, S., Meisel, T., Lacassie,
1033 J.B. & Voegelin, A.R. (2007). Evidence for a gradual rise of oxygen between 2.6 and 2.5
1034 Gafrom Mo isotopes and Re-PGE signatures in shales. *Geochimica et Cosmochimica*
1035 *Acta* **71**, 2417–2435.
1036
1037 Wilson, A.H. (2012). A chill sequence to the Bushveld Complex: insight into the first
1038 stage of emplacement and implications for the parental magmas. *Journal of Petrology*
1039 **53**, 1123–1168
1040
1041 Wingate, M.T.D., Campbell, I.H., Compston, W., and Gibson, G.M., 1998, Ion
1042 microprobe U-Pb ages for Neoproterozoic basaltic magmatism in southcentral Australia
1043 and implications for the breakup of Rodinia: Precambrian Research, v. 87, p. 135–159.
1044
1045 Yang, S., Maier, W.D., Lahaye,Y. & O'Brien, H. (2013). Strontium isotope
1046 disequilibrium of plagioclase in the Upper Critical Zone of the Bushveld Complex:

evidence for mixing of crystal slurries. *Contributions to Mineralogy and Petrology*, DOI 10.1007/s00410-013-0903-4

FIGURES

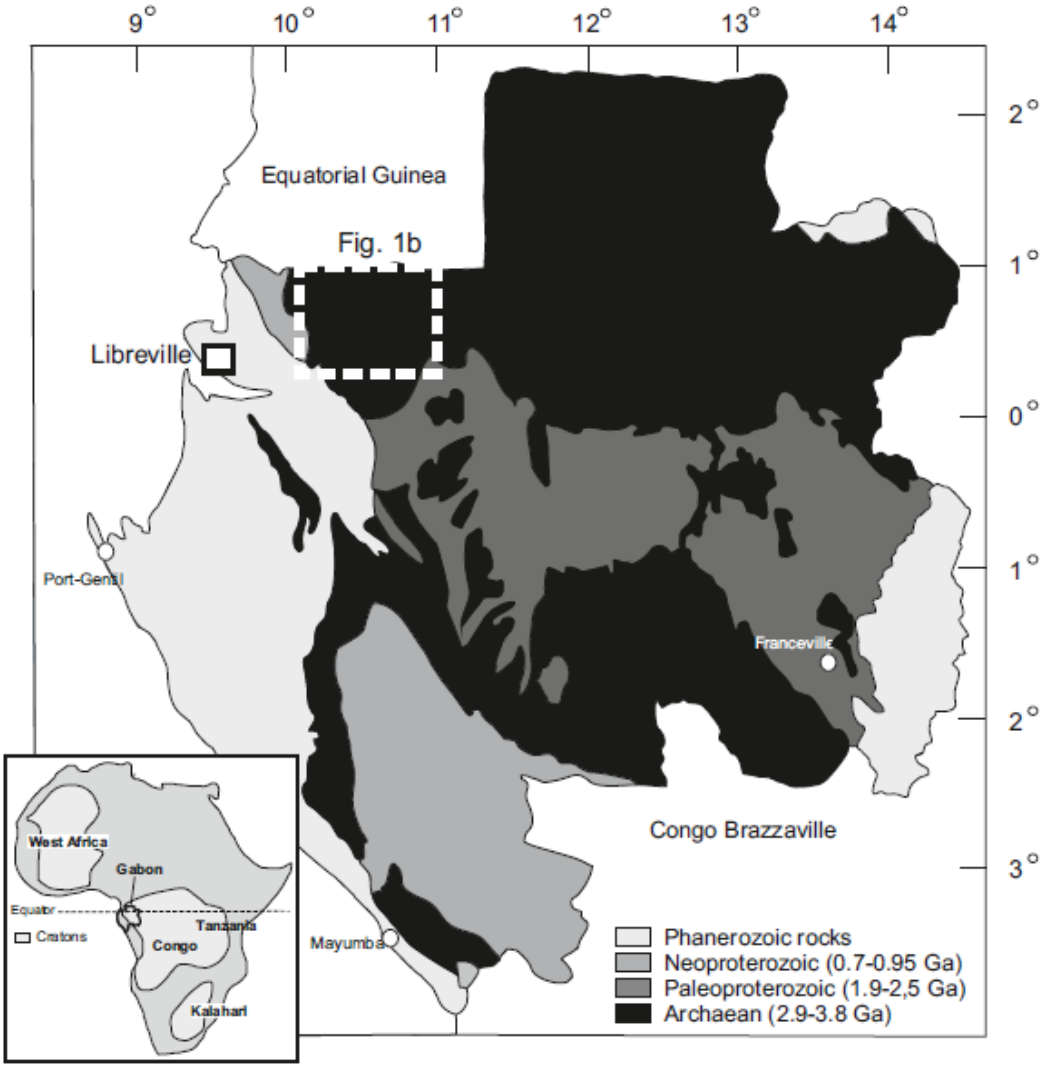

Fig. 1(a): Geological map of Gabon (modified after Chevalier et al. 2002). Insert shows segment enlarged in Fig. 1b. (b): Geological map of the Monts de Cristal Complex and its host rocks. Red line denotes outline of Monts de Cristal National Park. KG1-4 are individual blocks of Complex, and shaded areas with pink outline represent exploration focus areas. See insert of Fig. 1a for location.

1059

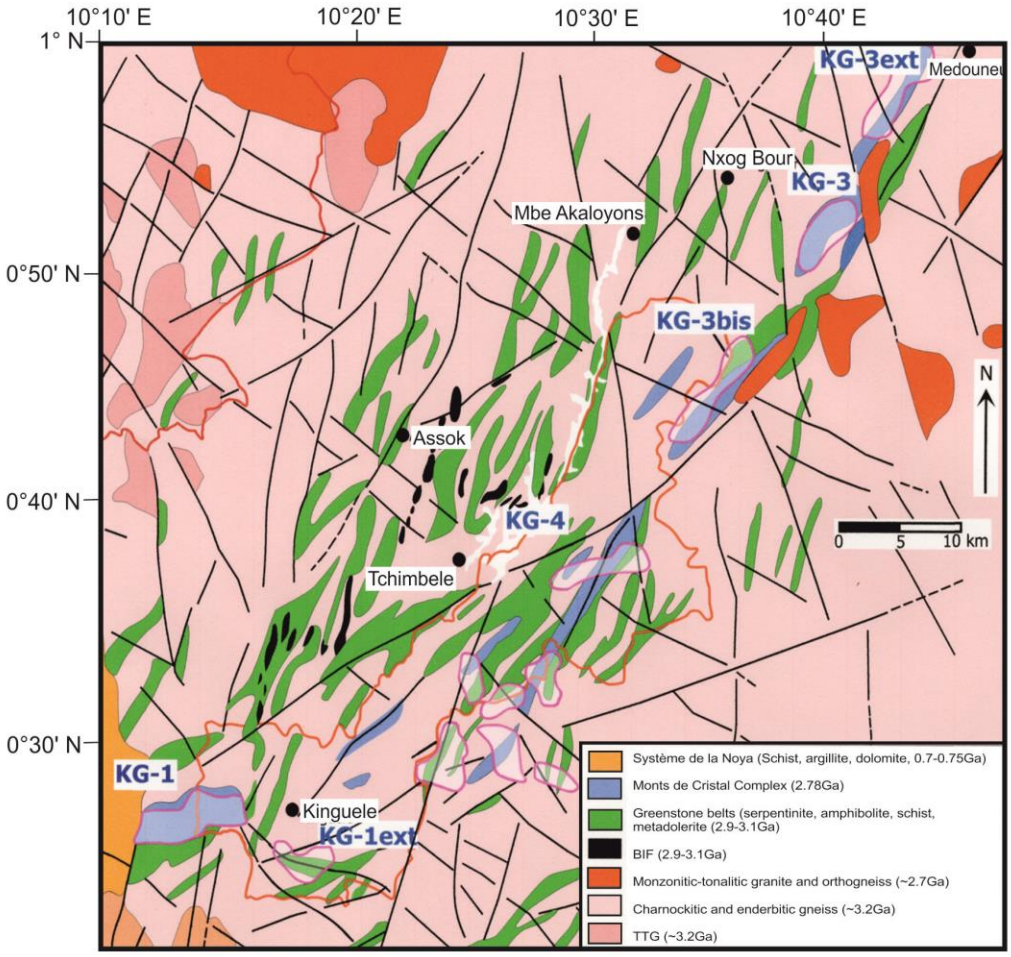

1060

1061 Fig. 2: Geological map of the KG1 body, showing sampling localities and drill core sites

1062 (denoted by stars, modified after Prendergast, 2009). Stippled line indicates a road.

1063 Coordinates are given in UTM system.

1064

Fig. 3: Photomicrographs of Monts de Cristal rocks. (a) Olivine pyroxenite showing olivine inclusions in orthopyroxene. Sample Olpx21. (b) Orthopyroxene adcumulate, sample Px21. (c) Orthopyroxenite mesocumulate. Zoning is indicated by dark coronas along rims of grains. Sample Px18. (d) Chromite clusters within orthopyroxene of orthopyroxenite adcumulate. Sample Px21. (e) Chromite clusters within altered inclusion in orthopyroxene. Sample Px21. (f) Norite, showing euhedral and subhedral orthopyroxene as well as cumulus and intercumulus plagioclase. Sample Px16. (g) Olivine gabbro, showing intercumulus olivine and clinopyroxene as well as acicular plagioclase crystals. Sample Dy18. (h) Olivine gabbro, showing large euhedral clinopyroxene oikocryst containing plagioclase chadacrysts. Sample Dy18. Length of scale bar in each panel is 1mm.

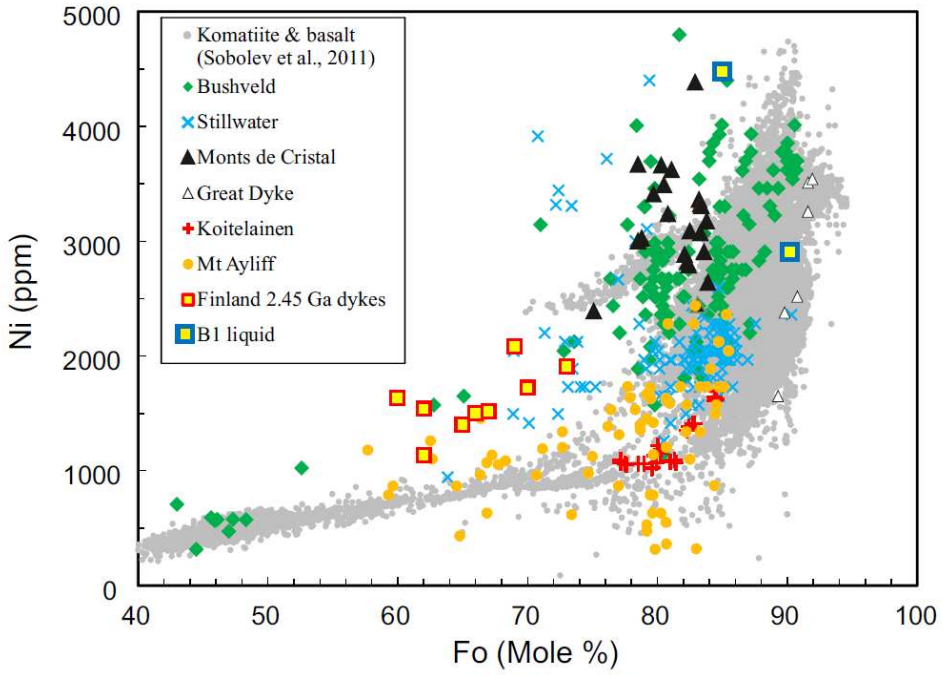

Fig. 4: Binary plot showing the variation of Fo and Ni contents of olivine in a number of layered intrusions. Note that the Monts de Cristal olivines have relatively high Ni contents compared to other intrusions with comparable Fo contents. Bushveld data are from Teigler and Eales (1996), Maier and Eales (1997) and Wilson (2012), Great Dyke data are from Wilson (pers. com., 2012), Koitelainen data are from Hanski (unpublished, pers. com., 2013), Stillwater data are from Raedeke (1982) and Barnes and Naldrett (1986), Mt Ayliff data are from Lightfoot and Naldrett (1983) and Lightfoot et al. (1984), and Finnish dykes are unpublished data of Fangfang Guo. Data for global komatiites and basalts are from Sobolev et al. (2011).

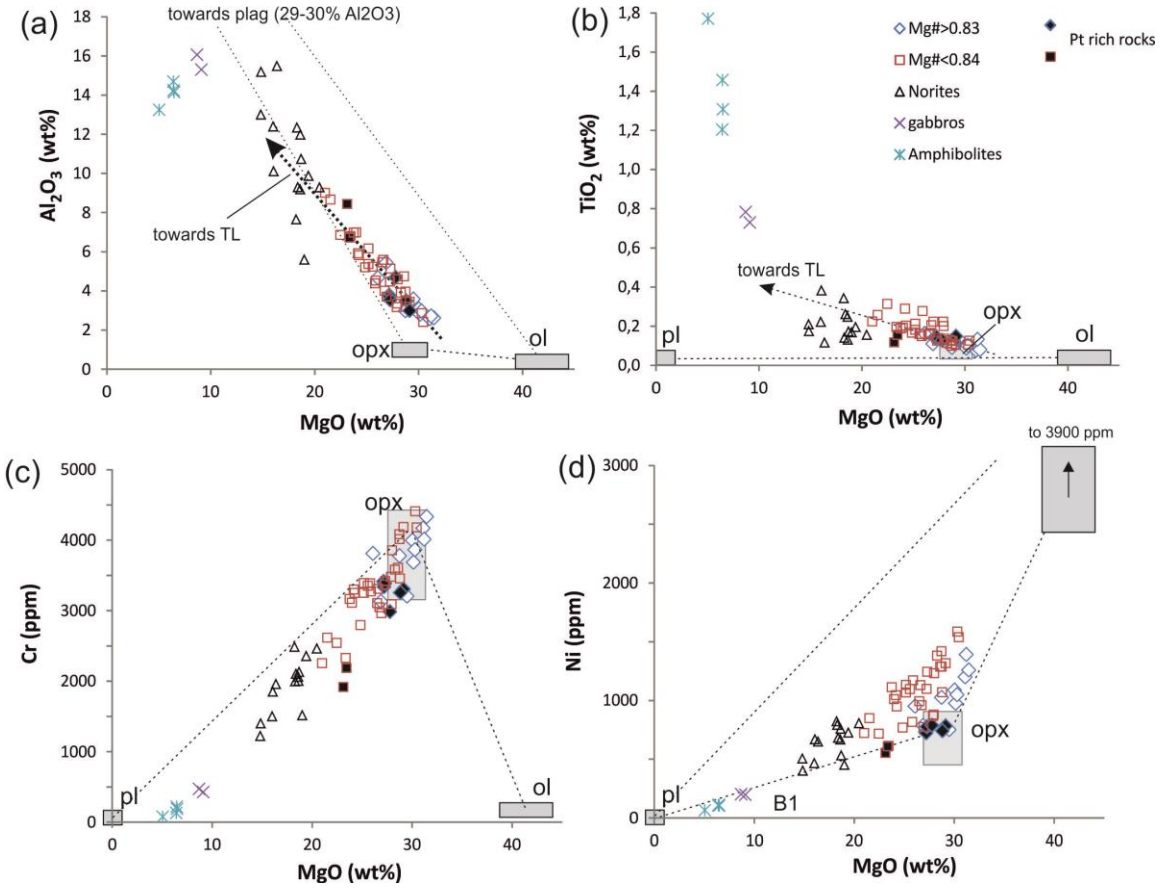

Fig. 5: Binary variation diagrams of (a) Al_2O_3, (b) TiO_2, (c) Cr, and (d) Ni, plotted vs MgO. Stippled arrows represent best fit lines through orthopyroxenites. Boxes linked by tielines indicate compositional ranges in analysed minerals.

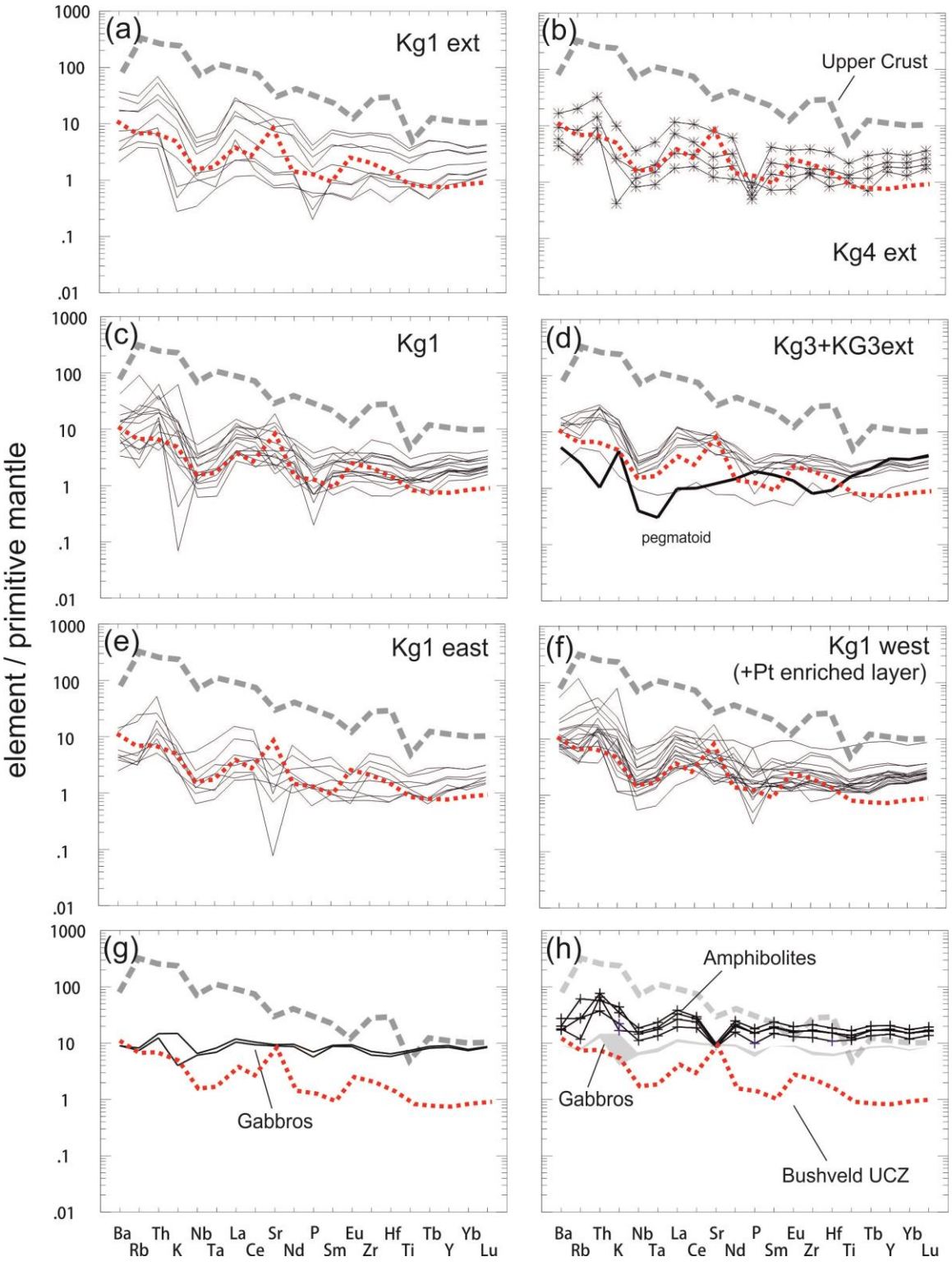

1094

1095 Fig. 6: Multi-element variation diagrams of lithophile trace elements. Data for Bushveld

1096 Upper Critical Zone are from Maier et al. (2013), and average Upper Crust is from

1097 Rudnick and Fountain (1995). Normalisation factors from McDonough and Sun (1995).

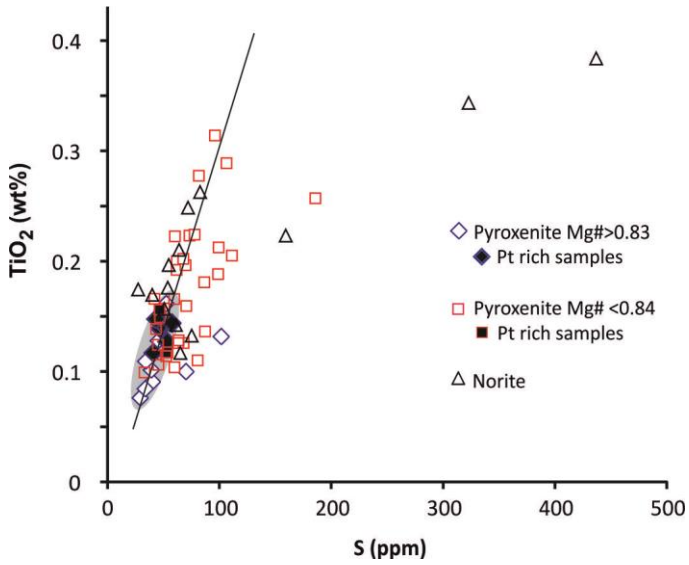

Fig. 7: Binary variation diagram of TiO_2 vs S. Regression line drawn through primitive orthopyroxenites (grey field, with exception of 2 samples) passes through origin and indicates approximately 100-150 ppm S in the putative trapped liquid at 0.4-0.5% TiO_2.

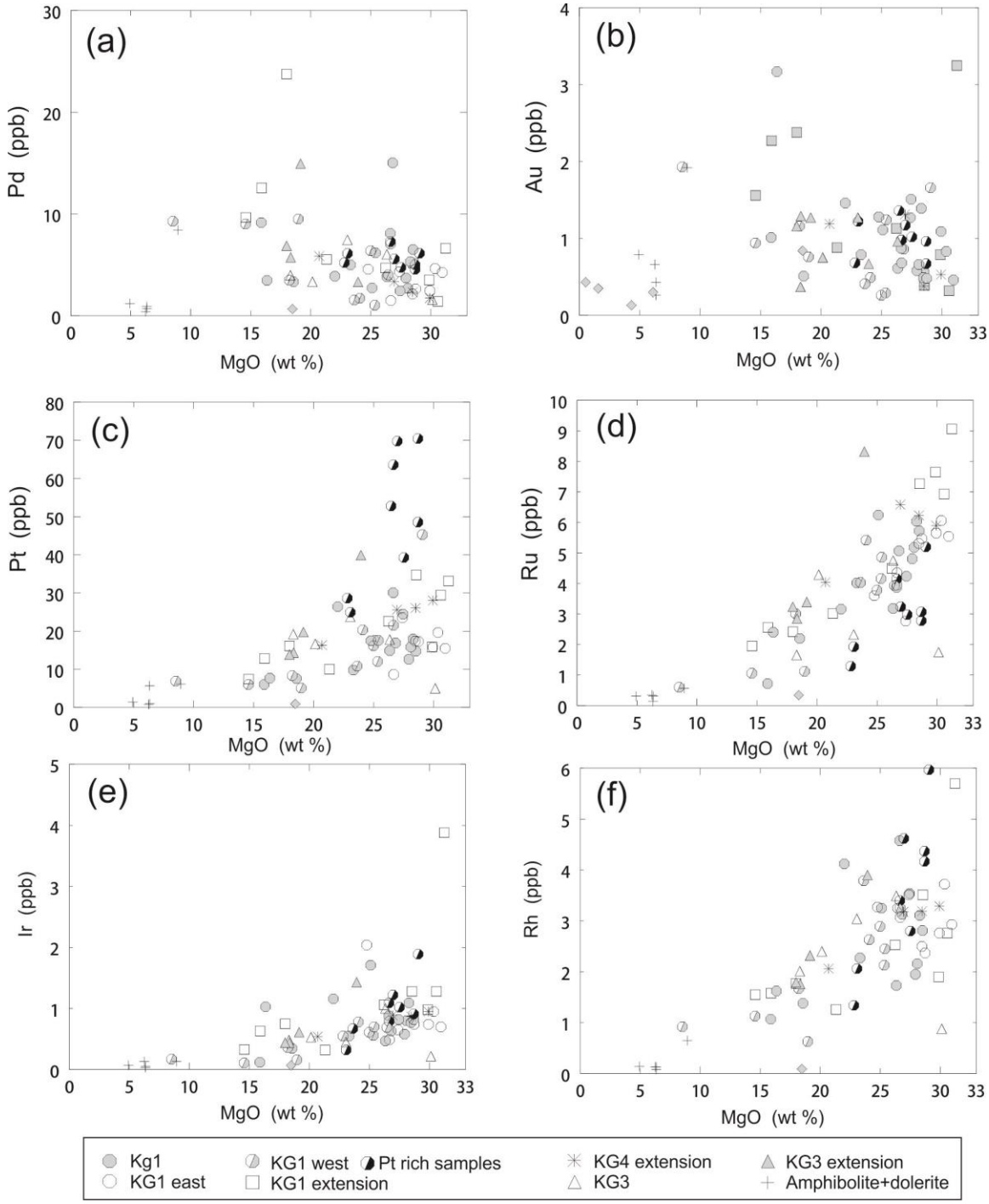

Fig. 8: Binary variation diagrams of chalcophile metals in various blocks of the Monts de Cristal Complex, plotted vs MgO. (a) Pd, (b) Au, (c) Pt, (d) Ru, (e) Ir, (f) Rh. Note negative correlations with MgO for Pd and Au, but positive correlations for Pt, Ru, Ir and Rh. See text for discussion.

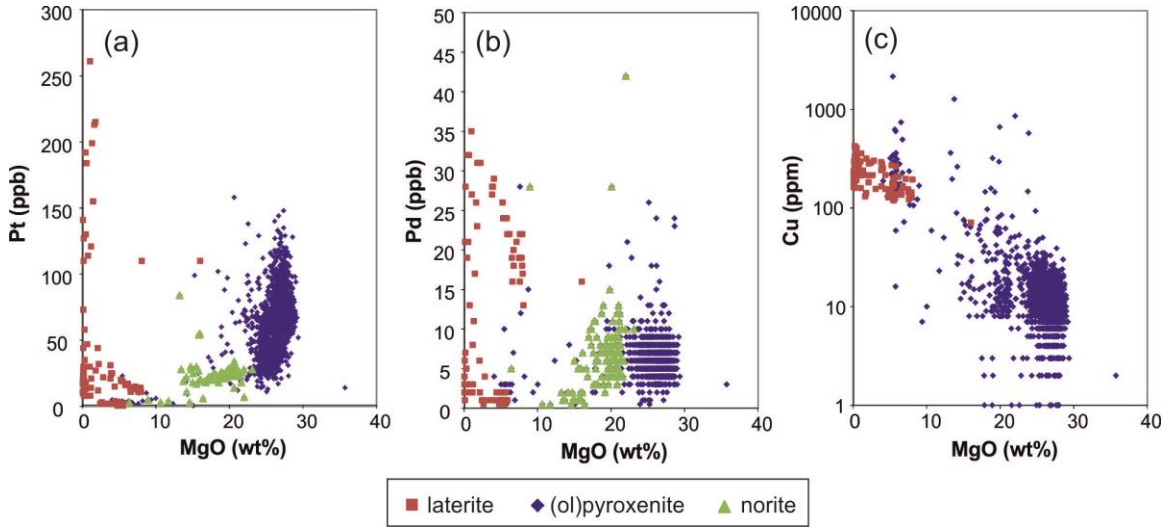

1109

1110 Fig. 9: Analyses of drill core samples plotted in binary variation diagrams vs MgO of (a)

1111 Pt, (b) Pd, and (c) Cu.

1112

1113

1114

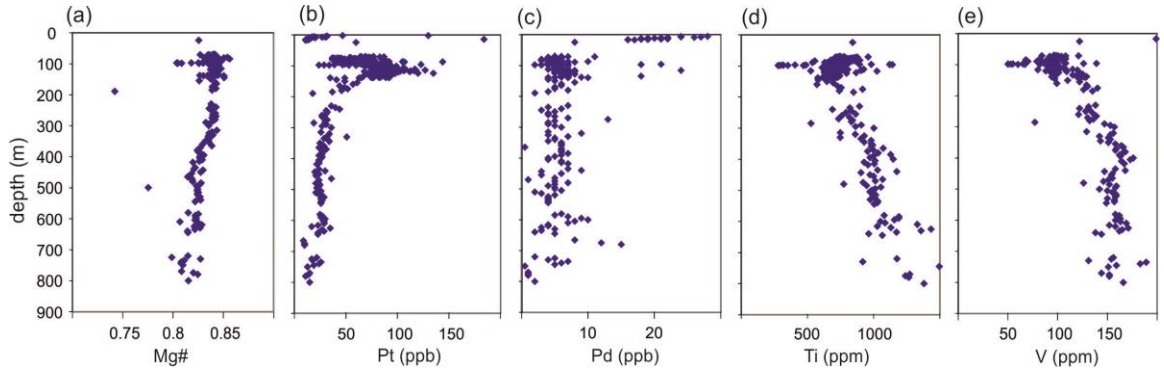

1115

1116 Fig. 10: Chemical data for drill core MPD-005

1117

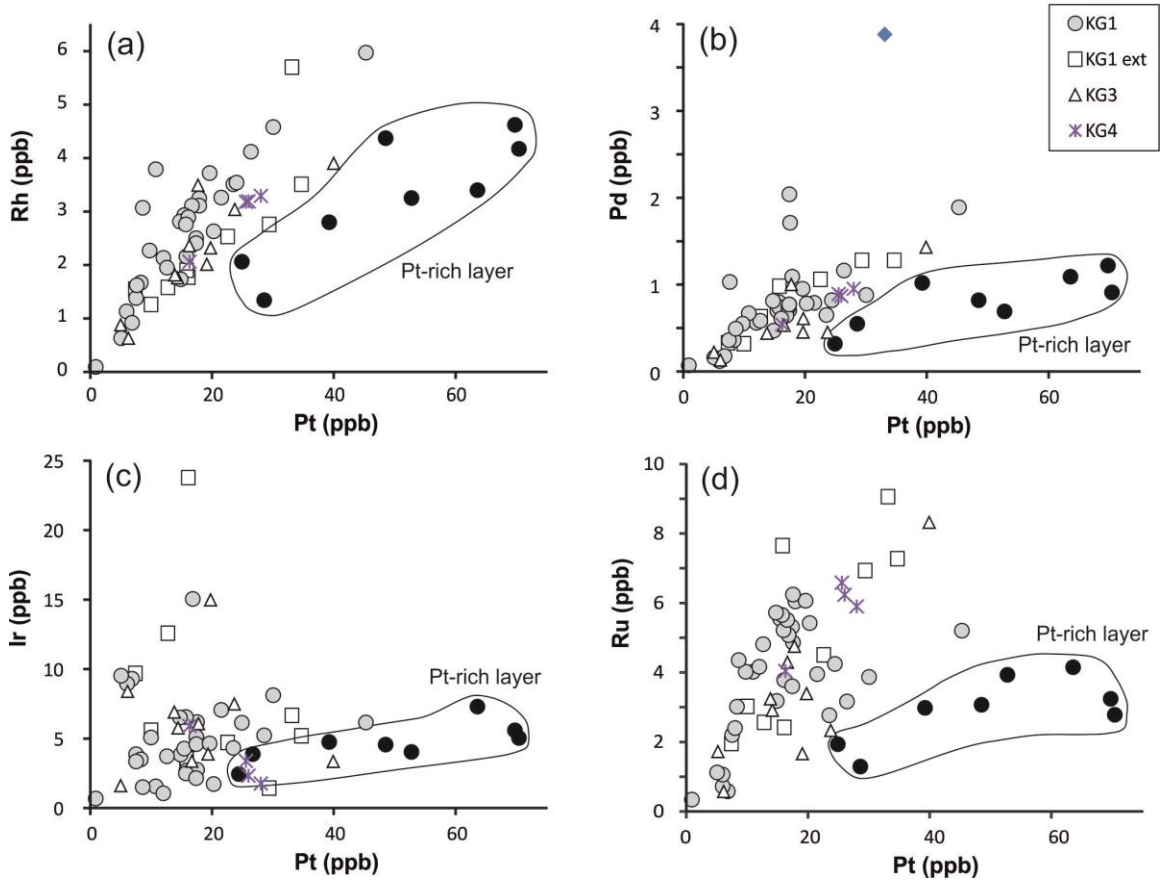

1118

1119 Fig. 11: (a-d) Binary variation diagrams for PGE. Note poor correlation between Pt and

1120 Pd, and high Pt/Pd ratios of most rocks. Outlined fields mark samples from Pt rich layer

1121 at KG1 west.

1122

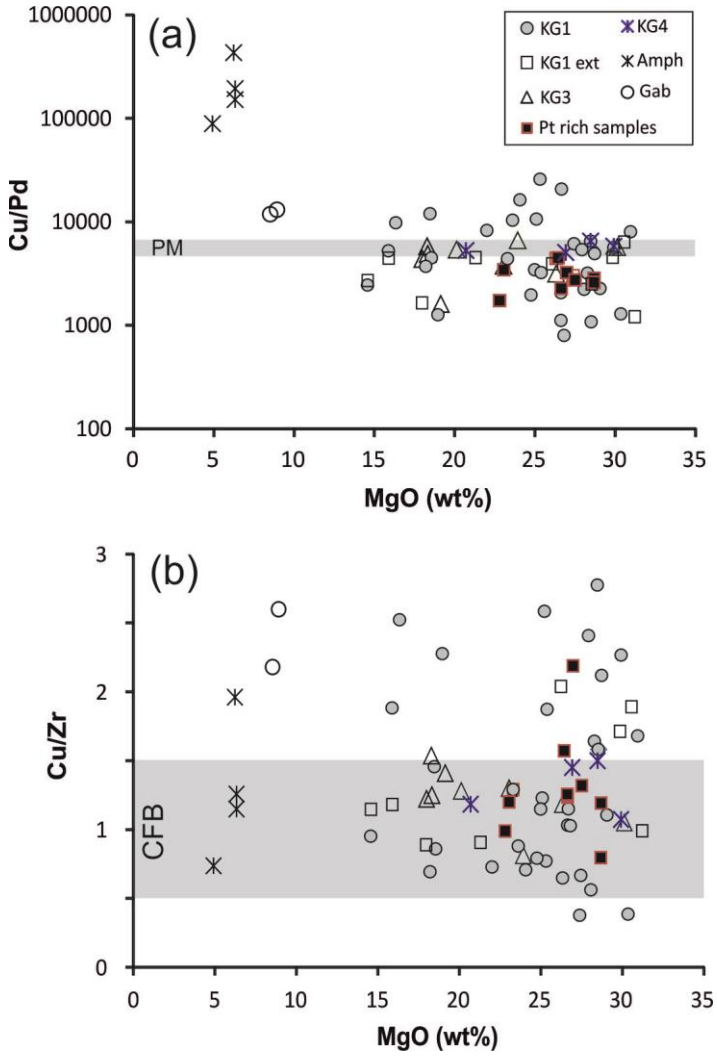

Fig. 12: Cu/Pd and Cu/Zr of Monts de Cristal rocks. Primitive mantle (PM) estimate is from Barnes and Maier (1999). Shaded bar in (b) represents range of South African continental flood basalts (CFB, from Maier et al., 2003).

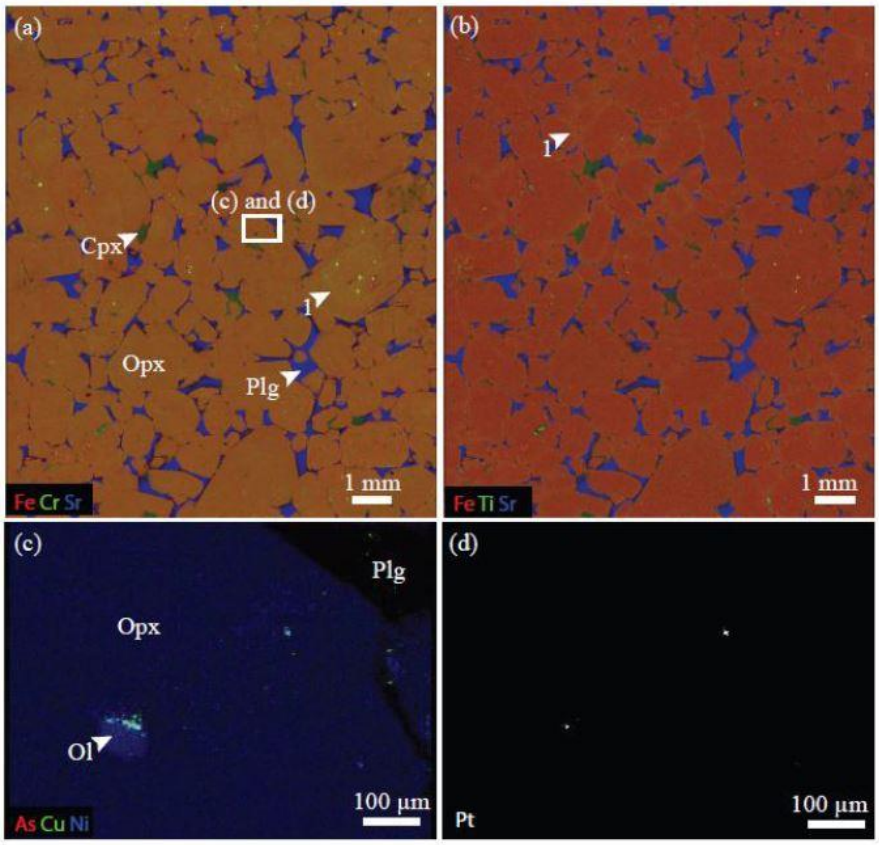

Fig. 13: a) and b) – three element false-colour RGB images of sample Px21. Each element is scaled to maximum values; Cr and Ti values are log transformed to enhance the compositonal range within the silicate phases. Note heterdacumulate texture of plagioclase oikocrysts (blue on both images) interstitial to orthopyroxene with minor intercumulus clinopyroxene (green on both images). Also note subtle complex internal zoning in Cr in some grains (grain 1 in image a) and fine rims of elevated Ti in image b in areas outside the plagioclase oikocrysts (point 1 in image b). Light green highlights on both images are small chromite inclusions, preferentially located in grains showing Cr zoning. (c) Three element image for As (red) – Cu (green) and Ni (blue) – light green areas indicate probable presence of Cu-Ni rich sulphide. One of these sulfide areas occupies the grain boundary between opx host and an olivine inclusion. Pt peaks in (d) correspond to coincident highs for As, within areas enriched in Cu and Ni, but not exactly matching Cu-Ni peaks. Pt corresponds exactly to As peak in each case. Note also presence of isolated small Cu-rich phases, probably sulphide, with no associated Pt or As, at opx margin.

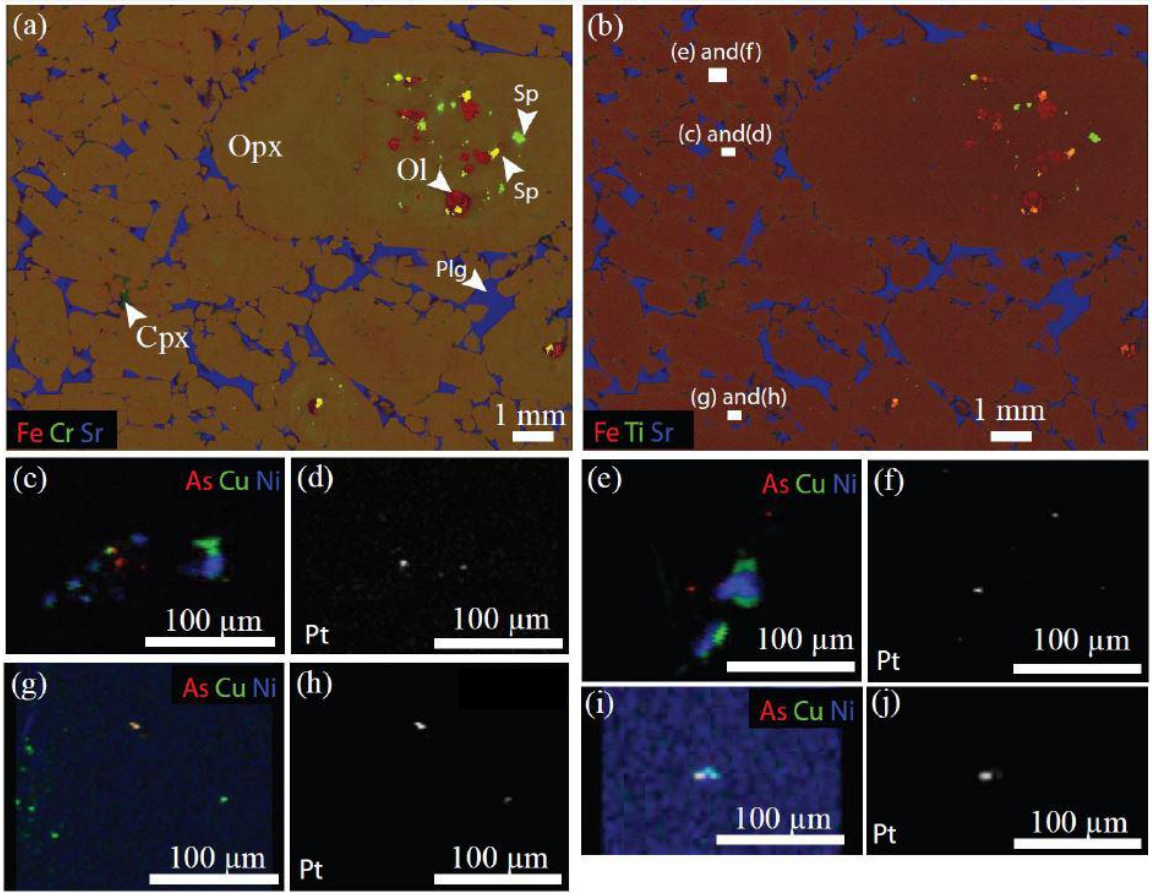

Fig. 14: Sample Px17A, with same combinations of elements as in Fig. 13a. Note abundant inclusions of olivine (red) and chromite (green) in Cr-zoned opx. No Pt grains were found in this grain, however. Enlarged areas show As-Cu-Ni three element maps as above, and corresponding single-element concentration maps for Pt. Note in all areas that Pt hits are associated with areas containing all three elements As, Cu and Ni, but the Pt peaks are very specifically associated with As, and do not necessarily occur directly within what appear to be sulphide aggregates. These aggregates are all occurring at or indistinguishably close to opx grain boundaries, but with no systematic relationship to plag oikocrysts.

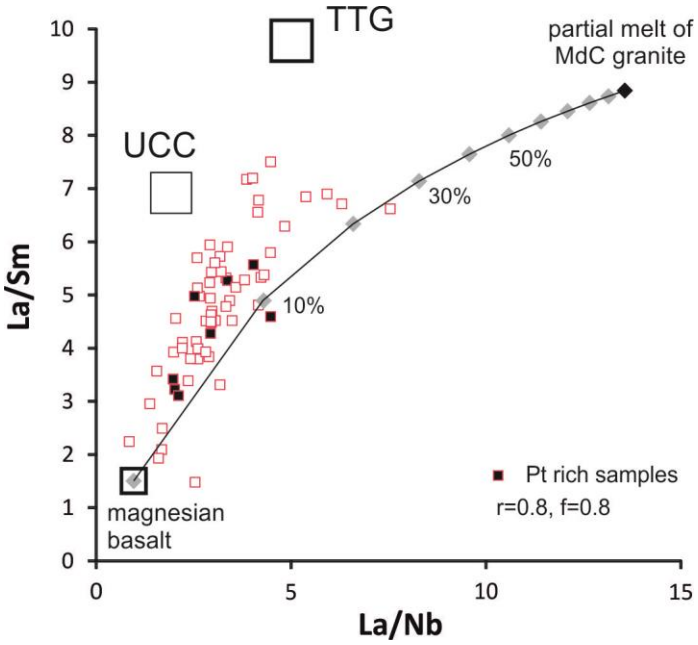

Fig. 15: Plot of La/Sm vs La/Nb for MdC rocks. Also plotted is average upper continental crust (Rudnick and Fountain, 1995) and average 3.0-3.5 Ga TTG (Martin et al., 2005). Solid line represents mixing line between magnesian basalt and a contaminated magma produced by AFC (r=0.8, f=0.8) of magnesian basalt with a 17% partial melt of MdC country rock granite. Trace element contents of magnesian basalt are assumed to be 4x that of primitive mantle (PM), with PM data taken from McDonough and Sun (1995). See text for further discussion.